XIV International Conference on Computational Plasticity. Fundamentals and Applications
COMPLAS XIV
E. Oñate, D.R.J. Owen, D. Peric & M. Chiumenti (Eds)

NUMERICAL MODELING OF STRAIN RATE HARDENING EFFECTS ON VISCOPLASTIC BEHAVIOR OF METALLIC MATERIALS

TIAGO DOS SANTOS[⋆], PEDRO A. R. ROSA[†], SAMIR MAGHOUS[‡], AND RODRIGO ROSSI[♮]

[⋆]Departamento de Engenharia Mecânica
Universidade Federal de Santa Maria
Santa Maria, RS, Brazil - 97105-900.
e-mail: tsantos.mec@gmail.com

[†]Instituto de Engenharia Mecânica
Instituto Superior Técnico, Universidade de Lisboa
Lisboa, Portugal - 1049-001.
e-mail: pedro.rosa@tecnico.ulisboa.pt

[‡]Departamento de Engenharia Civil
Universidade Federal do Rio Grande do Sul
Porto Alegre, RS, Brazil - 90040-020.
e-mail: rrossi@ufrgs.br

[♮]Departamento de Engenharia Mecânica
Universidade Federal do Rio Grande do Sul
Porto Alegre, RS, Brazil - 90046-902.
e-mail: rrossi@ufrgs.br

Key words: High strain rate effects, Finite strain, Elastic-viscoplastic material, Numerical algorithms, Finite elements.

Abstract. The main goal of the present work is to provide a finite strain elastic-viscoplastic framework to numerically account for strain, strain rate hardening, and viscous effects in cold deformation of metallic materials. The aim is to provide a simple and robust numerical framework capable of modeling the main macroscopic behavior associated with high strain rate plastic deformation of metals. In order to account for strain rate hardening effects at finite strains, the hardening rule involves a rate dependent saturation hardening, and it accounts for linear hardening prevailing at latter deformation stages. The numerical formulation, finite element implementation, and constitutive modeling capabilities are assessed by means of decremental strain rate testing and constant strain rate loading followed by stress relaxation. The numerical results have demonstrated the overall framework can be an efficient numerical tool for simulation of plastic deformation processes where strain rate history effects have to be accounted for.

1 Introduction

High strain rates and large strains are present in several engineering applications of polycrystalline metallic materials, such as manufacturing (e.g. high speed forming and machining of metals), machine tools design, analysis of structural crashworthiness in the automotive and aerospace industries, terminal ballistics research for safety and military activities, among several others. Modeling of these applications requires large scale simulations and adequate constitutive predictions.

To properly predict high strain rate straining of metals, a constitutive framework should account for deformation and loading history effects. For example, the hardening response of FCC metals is strongly rate-dependent at high velocity conditions [1, 2, 3, 4, 5]. In summary, a high strain rate model has to comply with adequate constitutive features accounting for the main plastic effects on the flow stress and material hardening responses. However, while incorporating suitable constitutive capabilities, a constitutive model to be employed in large scale engineering computations has to be simple enough to be experimentally and numerically "attractive". From a constitutive point of view, physically-based models employing macroscopic [6, 7, 8, 9] or microscopic frameworks [10, 11, 12] allow for a detailed description of both material behavior and its current state, thus providing an appropriate framework for capturing loading-history effects. However, in contrast physically-based models require complex optimization algorithms and large computational efforts to find associated model constants, see for instance comments provided in references [8, 13]. In addition, due to formulation complexity, physically-based approaches are less numerically efficient than phenomenological procedures, thus requiring more computational time and efforts in numerical simulation of large scale problems. Concerning the formulation simplicity, the lower number of material parameters and of experiments to identify them, many researchers [14, 15, 16, 17] have proposed semi-physical constitutive models, once a detailed physical description increase the model complexity and the number of constants to be adjusted.

In large scale simulations, accurate, efficient, and robust numerical tools are mandatory in order to guarantee appropriate predictions and to save computational time. In a global standpoint, the finite element (FE) method has proved to be a suitable tool in solving nonlinear initial boundary value problems [18, 19]. The whole numerical framework must integrate the set of nonlinear constitutive equations into a FE context, requiring the fulfillment of two main tasks at the material level: (i) the update of stress and state variables from a given strain increment, and (ii) the calculation of consistent tangent modulus to be used in the global implicit FE scheme, thus preserving quadratic convergence rate of *Newton*-type solution algorithms [18, 19]. Aiming at accomplishing these tasks and improving the computational efficiency, several viscoplastic implicit integration algorithms for large strain problems have been proposed [20, 21, 22, 23]. Mostly of the large strain formulations are based on the well-known multiplicative decomposition of the deformation gradient [24, 25], and generally associated algorithmic formulations preserves material objectivity.

Aiming at contributing to the constant search for models combining both constitu-

tive adequacy and computational efficiency, the present work has the goal of providing a simple and efficient numerical framework capable of modeling the main macroscopic behavior associated with high strain rate plastic deformation of metals at room temperature. The work concerns numerical formulation and simulations where advantage is taken of a constitutive model previously presented [26], which proved to be suitable for this task. Adopting a simplified semi-physical approach allows to maintain the corresponding computational efficiency associated with phenomenological models [27, 28, 29, 30] while incorporating adequate constitutive capabilities, such as strain rate history effects, in simulations where high velocity plastic features have to be taken into account.

The present constitutive formulation adopts a *von Mises* plasticity employing a strain-rate-history-dependent isotropic hardening, whose evolution equations follow the viscoplastic framework of *Perzyna* [31, 27], in which the inelastic evolution is given in terms of an *overstress* function. Specifically, the isotropic hardening is taken into account by a single scalar internal variable, which can be interpreted as an effective microstructural feature [15, 26]. The stress hardening variable is composed by two main contributions, namely A_1 and A_2. The first is associated with dislocations storage, and its evolution is based on physical aspects as dislocation generation and annihilation mechanisms. The second contribution, A_2, is linked to geometric hardening mechanisms associated with deformation Stage IV, in which the hardening is mainly induced by granular misorientations. It is worth mentioning that a formulation following an overstress description needs an explicit definition of the strain rate, and it presents some constitutive differences compared to other viscoplastic contexts as the consistency model [32, 33]. For example, concerning the overstress description, plastic deformation increase during unloading while overstress function has a nonzero value [22, 13]. However, within the present approach this constitutive distinction is not so relevant once it is intended to monotonic loading, thus justifying the employment of an overstress formulation, as well as a pure isotropic hardening. From an overall point of view, the elastic-viscoplastic model presented in [26] is embedded into a finite strain framework, which adopts a total *Lagrangian* description and employ the classical multiplicative decomposition of the deformation gradient into its viscoplastic and elastic parts. An isotropic material is considered, whose constitutive formulation is given in terms of the logarithmic deformation measure and the rotated *Kirchhoff* stress. The elastic response is assumed to be linear and given by the *Hencky* hyperelastic model. The numerical approach follows ideas presented in references [34, 21], where a standard elastic predictor-plastic corrector algorithm is employed. However, to incorporate rate dependent hardening features, additional incremental equations arise within the return mapping step. Seeking for computational efficiency, an analytical consistent tangent operator is obtained from linearization of the return mapping equations.

The work is organized as follows. Section 2 presents an overview of the constitutive model adopted [26]. In this section, the global boundary value problem in its strong and weak form is stated. From linearization of weak formulation the continuum material tangent modulus is identified. Section 4 outlines the local incremental constitutive formulation, recalling the well-known elastic predictor-plastic corrector algorithm. Also, the consistent tangent modulus is given in a closed-form. In the sequel, with the aim of show-

ing the model constitutive capabilities, and highlighting the main macroscopic material behavior associated with loading history effects, a numerical decremental strain rate test and a constant strain rate loading followed by stress relaxation testing are performed in Sec. 5, employing the model parameters obtained in [26] for an annealed OFHC copper. Numerical results are compared with experimental data available in the literature [3, 35]. Furthermore, as a non-homogeneous deformation example, a billet upsetting is simulated. Convergence analyzes, considering both frictionless and frictional billet upsetting cases, are also performed. Our conclusions and comments are given in Sec. 6. Tangent terms required into return mapping algorithm are given in A and the analytical consistent tangent modulus is derived in B.

2 Overview of constitutive model

We adopt the classical multiplicative[1] decomposition of the deformation gradient [24, 36]

$$\boldsymbol{F} = \boldsymbol{F}^e \boldsymbol{F}^{vp}, \tag{1}$$

where $\boldsymbol{F} = \frac{\partial \boldsymbol{\varphi}(\boldsymbol{X},t)}{\partial \boldsymbol{X}}$, $\boldsymbol{\varphi}$ being the displacement function which maps an initial point $\boldsymbol{X} \in \Omega_0$ onto a current one $\boldsymbol{x} \in \Omega$ at time t, such that $\boldsymbol{x} = \boldsymbol{\varphi}(\boldsymbol{X}, t)$. Terms $\boldsymbol{F}^e$ and $\boldsymbol{F}^{vp}$ are the elastic and viscoplastic part of $\boldsymbol{F}$. By adopting decomposition (1), the specific *Helmholtz* free-energy can be split [37],

$$\psi = \psi^e(\boldsymbol{E}^e) + \psi^{vp}(\alpha), \tag{2}$$

into its elastic ψ^e and inelastic ψ^{vp} parts. Tensor $\boldsymbol{E}^e = \ln(\boldsymbol{U}^e)$ is the *Hencky* elastic strain with $\boldsymbol{U}^{e^2} = (\boldsymbol{F}^e)^T \boldsymbol{F}^e$ and $\boldsymbol{F}^e = \boldsymbol{F}\boldsymbol{F}^{vp^{-1}}$. A single internal variable α is assumed to describe irreversible material behavior (see for instance references [38, 39, 40, 37]). In this work we assume standard quadratic forms

$$\psi^e = \frac{1}{2}\boldsymbol{E}^e : \mathbb{D}^e : \boldsymbol{E}^e \;\text{ and }\; \psi^{vp} = \frac{1}{2}H\alpha^2, \tag{3}$$

where $\mathbb{D}^e$ is a symmetric positive-definite forth-order elastic tensor and $H \geq 0$ is the hardening modulus. Furthermore, isotropic elasticity is considered in subsequent analysis:

$$\mathbb{D}^e = 2\mu\mathbb{I} + \left(\kappa - \frac{2}{3}\mu\right)\boldsymbol{I} \otimes \boldsymbol{I}, \tag{4}$$

where $\mathbb{I}$, $\boldsymbol{I}$, μ and κ are the fourth-order and the second-order identity tensors, the shear and bulk modulus, respectively. Components of $\mathbb{I}$ are $I_{ijkl} = \frac{1}{2}(\delta_{ik}\delta_{jl} + \delta_{il}\delta_{jk})$ with δ_{ij} denoting the *Kronecker*'s symbol.

Thermodynamic forces must obey the constitutive relations

$$\bar{\boldsymbol{\tau}} = \rho_0 \frac{\partial \psi^e}{\partial \boldsymbol{E}^e} = \mathbb{D}^e : \boldsymbol{E}^e \;\text{ and }\; A = \rho_0 \frac{\partial \psi^{vp}}{\partial \alpha} = H\alpha, \tag{5}$$

[1] Along this work single contractions between second-order tensors are omitted, i.e., $\boldsymbol{S} \cdot \boldsymbol{T} = \boldsymbol{S}\boldsymbol{T}$, in components $(\boldsymbol{S}\boldsymbol{T})_{ij} = S_{ik}T_{kj}$.

where $\bar{\boldsymbol{\tau}}$ is the rotated *Kirchhoff* stress [34]. The latter is related to the *Kirchhoff* stress tensor $\boldsymbol{\tau}$ by means of the right rotation tensor $\boldsymbol{R} = \boldsymbol{F}\boldsymbol{U}^{-1}$ with $\boldsymbol{U}^2 = \boldsymbol{F}^T\boldsymbol{F}$, such that $\bar{\boldsymbol{\tau}} = \boldsymbol{R}^T\boldsymbol{\tau}\boldsymbol{R}$. It is recalled that $\boldsymbol{\tau}$ and the *Cauchy* stress tensor $\boldsymbol{\sigma}$ are related through $\boldsymbol{\tau} = J\boldsymbol{\sigma}$ with $J = \det(\boldsymbol{F})$. Parameter A stands for the isotropic hardening associated with α. For sake of simplicity, in what follows we adopt a *von Mises* yield criterion together with an isotropic hardening A

$$f(\bar{\boldsymbol{\tau}}, A) = \left\|\bar{\boldsymbol{\tau}}^D\right\| - \sqrt{\frac{2}{3}}(\sigma_y + A), \tag{6}$$

where $\left\|\bar{\boldsymbol{\tau}}^D\right\| = \sqrt{\bar{\tau}_{ij}^D\bar{\tau}_{ij}^D}$, $\bar{\boldsymbol{\tau}}^D = \bar{\boldsymbol{\tau}} - \frac{1}{3}\mathrm{tr}(\bar{\boldsymbol{\tau}})\boldsymbol{I}$ is the deviatoric part of $\bar{\boldsymbol{\tau}}$ and σ_y is the initial yield stress.

2.1 Evolution equations

The viscoplastic strain rate $\bar{\boldsymbol{D}}^{vp} = \mathrm{sym}\left(\dot{\boldsymbol{F}}^{vp}\boldsymbol{F}^{vp^{-1}}\right)$ is given by the evolution equation[2]

$$\bar{\boldsymbol{D}}^{vp} = \dot{\lambda}\frac{\partial f}{\partial \bar{\boldsymbol{\tau}}} \tag{7}$$

where the viscoplastic multiplier $\dot{\lambda}$ expresses as [31, 27]

$$\dot{\lambda} = \frac{1}{\vartheta}\Theta(\langle f\rangle, A). \tag{8}$$

In the above equality, operator $\langle x\rangle \equiv \frac{1}{2}(x + |x|)$ denotes the *Macaulay* brackets, $\vartheta \geq 0$ is the material viscosity parameter and $\Theta \geq 0$ is the *overstress* function which should be convex with relation to both f and A. Hardening variable A is given by

$$A = A_1 + cA_\infty\epsilon, \tag{9}$$

where $c \geq 0$ is a material parameter, A_∞ is the saturation work hardening, A_1 is associated with hardening induced by dislocation storage and its arrangement in dislocation cells, and term $cA_\infty\epsilon$ is related to geometric hardening due to cellular and granular misorientations. Evolution of first term is given by

$$\dot{A}_1 = H_1\left(1 - \frac{A_1}{A_\infty}\right)\dot{\epsilon}, \tag{10}$$

where H_1 is the hardening rate and

$$\dot{\epsilon} = \sqrt{\frac{2}{3}}\left\|\bar{\boldsymbol{D}}^{vp}\right\| \geq 0 \tag{11}$$

[2]Under the hypothesis of inelastic isotropy, without loss in generality, a irrotational viscoplastic flow may be assumed [21, 41]: $\bar{\boldsymbol{W}}^{vp} = \mathrm{skew}\left(\dot{\boldsymbol{F}}^{vp}\boldsymbol{F}^{vp^{-1}}\right) = \boldsymbol{0}$.

is the accumulated viscoplastic strain rate. Assuming constant value for $\dot{\epsilon}$, evolution equation (10) is directly integrated leading to a *Voce* hardening law [42],

$$\frac{A_1 - A_\infty}{A_{1_i} - A_\infty} = \exp\left[-\delta\left(\epsilon - \epsilon_i\right)\right]. \tag{12}$$

Parameters A_{1_i} and ϵ_i stand for the initial values of A_1 and ϵ, respectively, and $\delta = \frac{H_1}{A_\infty}$. In the present formulation we assume the ratio $\delta = \frac{H_1}{A_\infty}$ as constant, and a rate dependence will be assigned to A_∞. Combination of Eqs. (9) and (12) yields

$$A = A_i + A_\infty c\left(\epsilon - \epsilon_i\right) + \left[A_\infty\left(1 + c\epsilon_i\right) - A_i\right]\left\{1 - \exp\left[-\delta\left(\epsilon - \epsilon_i\right)\right]\right\}, \tag{13}$$

where A_i is the initial value of A. Considering that $A_i = \epsilon_i = 0$, Eq. (13) reduces to

$$A = A_\infty\left[1 + c\epsilon - \exp\left(-\delta\epsilon\right)\right], \tag{14}$$

which is a modified *Voce* hardening law. Hardening equation (13), obtained based upon the assumption of constant rate $\dot{\epsilon}$, is usefull to be employed within numerical algorithms in which inelastic strain rate is assumed within each increment. Now, Eq. (14) is intended to monotonic loading applications starting from a non-deformed state.

The following *a priori* rate-dependent form is postulated for A_∞, see reference [26]:

$$A_\infty = \left[1 - \beta\left(\dot{\epsilon}\right)\right] A_\infty^{lwr} + \beta\left(\dot{\epsilon}\right) A_\infty^{up}, \tag{15}$$

where A_∞^{lwr} is the *quasi*-static value of A_∞ measured at a lower reference rate $\dot{\epsilon}_{lwr} \ll 1$ and A_∞^{up} is the value associated with upper reference strain rate $\dot{\epsilon}_{up} \gg 1$. Function β is given by

$$\beta\left(\dot{\epsilon}\right) = \left(\frac{\dot{\epsilon} - \dot{\epsilon}_{lwr}}{\dot{\epsilon}_{up} - \dot{\epsilon}_{lwr}}\right)^{\xi}, \tag{16}$$

which obviously satisfies $\beta\left(\dot{\epsilon}_{lwr}\right) = 0$ and $\beta\left(\dot{\epsilon}_{up}\right) = 1$, scalar $\xi > 0$ is a material constant.

In the present work, a viscoplastic constitutive function $\Theta\left(\langle f\rangle, A\right)$ based on that proposed in [28] is adopted,

$$\vartheta\dot{\lambda} = \Theta\left(\langle f\rangle, A\right) = \left(\frac{\langle f\rangle + R}{R}\right)^m - 1. \tag{17}$$

For $f \geq 0$, the inverse of Θ with respect to $\dot{\lambda}$ and f reads

$$f = \Theta^{-1}\left(\dot{\lambda}, A\right) = R\left[\left(1 + \vartheta\dot{\lambda}\right)^{\frac{1}{m}} - 1\right], \tag{18}$$

where $\frac{1}{m}$ is the rate sensitivity parameter and $R\left(A\right)$ is a characteristic size of the yield locus, which is expressed as

$$R\left(A\right) = \sqrt{\frac{2}{3}}\left(\sigma_y + A\right) \tag{19}$$

in the case of *von Mises* yield criterion (6).

3 Incremental formulation and finite element implementation

Let Ω_0 be the initial configuration of a body with boundary $\partial\Omega_0$ and particles labeled $\boldsymbol{X} \in \Omega_0$. An ordinary loading is defined by a prescribed body force $\bar{\boldsymbol{b}}$ in Ω_0, a prescribed surface traction $\bar{\boldsymbol{t}}$ acting on Γ_0^t and a displacement $\bar{\boldsymbol{u}}$ prescribed on Γ_0^u, with $\partial\Omega_0 = \Gamma_0^t \cup \Gamma_0^u$ and $\Gamma_0^t \cap \Gamma_0^u = \emptyset$. Deformed body is defined by the current configuration Ω with boundary $\partial\Omega$ and particles $\boldsymbol{x} \in \Omega$, being the displacement field given by $\boldsymbol{u} = \boldsymbol{x} - \boldsymbol{X}$. The mechanical problem in its strong form, disregarding inertia effects, can be stated as follows: Find $\boldsymbol{u}$ such that

$$\left\{\begin{array}{rcl} \mathrm{div}\boldsymbol{P} + \bar{\boldsymbol{b}} &=& \boldsymbol{0} \text{ on } \Omega_0 \\ \boldsymbol{P}\boldsymbol{m} &=& \bar{\boldsymbol{t}} \text{ on } \Gamma_0^t \\ \boldsymbol{u} &=& \bar{\boldsymbol{u}} \text{ on } \Gamma_0^u \end{array}\right. , \tag{20}$$

where $\boldsymbol{P} = \boldsymbol{\tau}\boldsymbol{F}^{-T}$ is the first *Piola-Kirchhoff* stress tensor and $\boldsymbol{m}$ is the unit outward normal vector at $\boldsymbol{X} \in \partial\Omega_0$. Based on strong form given by Eqs. (20), the weak formulation, employing the virtual work principle, consists of finding $\boldsymbol{u}$ satisfying

$$\mathscr{R}\left(\boldsymbol{u}, \hat{\boldsymbol{u}}\right) = \int_{\Omega_0} \boldsymbol{P}\left(\boldsymbol{u}\right) : \nabla_{\boldsymbol{X}} \hat{\boldsymbol{u}} dV - \int_{\Omega_0} \rho_0 \bar{\boldsymbol{b}} \cdot \hat{\boldsymbol{u}} dV - \int_{\Gamma_0^t} \bar{\boldsymbol{t}} \cdot \hat{\boldsymbol{u}} dA = 0, \tag{21}$$

$\forall \hat{\boldsymbol{u}} \in \mathscr{W}_p^1\left(\Omega_0\right)$, where $\nabla_{\boldsymbol{X}}\left(\cdot\right)$ denotes the material derivative of field $(\cdot)$ and $\hat{\boldsymbol{u}}$ is the virtual displacement vector field.

3.1 Linearized incremental Boundary Value Problem

The incremental strategy adopted herein consists of subdividing the whole time interval of interest $\mathscr{I}$ into $N > 0$ subintervals $(t_n, t_{n+1}]$: $\mathscr{I} = \bigcup_{n=1}^{N} (t_n, t_{n+1}]$. Adopting an implicit solution scheme, for a time subinterval $(t_n, t_{n+1}]$ Eq. (21) have to be satisfied at t_{n+1}, and the increment associated with a given quantity $(\cdot)$ is given by $\Delta(\cdot) := (\cdot)_{n+1} - (\cdot)_n$, being $(\cdot)_{n+1}$ and $(\cdot)_n$ the values at instants t_{n+1} and t_n, respectively. Following this incremental strategy, the internal variables $\boldsymbol{\alpha}_n\left(\boldsymbol{X}\right)$, the displacement $\boldsymbol{u}_n\left(\boldsymbol{X}\right)$, as well as the stress $\boldsymbol{P}_n\left(\boldsymbol{X}\right)$ fields are assumed to be known at the initial time instant t_n and to comply with Eq. (21). The incremental equilibrium problem corresponding to a time subinterval $(t_n, t_{n+1}]$ consists therefore of finding the current displacement field $\boldsymbol{u}_{n+1}\left(\boldsymbol{X}\right) \in \mathcal{K}_{n+1}$, satisfying

$$\mathscr{R}\left(\boldsymbol{u}_{n+1}, \hat{\boldsymbol{u}}\right) = \int_{\Omega_0} \boldsymbol{P}_{n+1} : \nabla_{\boldsymbol{X}} \hat{\boldsymbol{u}} dV - \int_{\Omega_0} \rho_0 \bar{\boldsymbol{b}}_{n+1} \cdot \hat{\boldsymbol{u}} dV - \int_{\Gamma_0^t} \bar{\boldsymbol{t}}_{n+1} \cdot \hat{\boldsymbol{u}} dA = 0, \;\; \forall \hat{\boldsymbol{u}} \in \mathscr{W}_p^1\left(\Omega_0\right), \tag{22}$$

where $\mathcal{K}_{n+1}$ is the set of kinematically admissible displacements at t_{n+1}. Within the present numerical framework, the local integration algorithm provides an incremental stress function $\bar{\boldsymbol{P}}$ given in terms of $\boldsymbol{F}_{n+1}$ and $\boldsymbol{\alpha}_n$ [19]: $\boldsymbol{P}_{n+1} = \bar{\boldsymbol{P}}\left(\boldsymbol{F}_{n+1}, \boldsymbol{\alpha}_n\right)$.

Solving Eq. (22) by means of an iterative procedure, such as the Newton-Raphson method, at iteration $k+1$ one has to determine a displacement increment $\Delta\boldsymbol{u}_{n+1}^{k+1}$ satisfying condition

$$\mathscr{R}\left(\boldsymbol{u}_{n+1}^{k+1}, \hat{\boldsymbol{u}}\right) = \mathscr{R}\left(\boldsymbol{u}_{n+1}^{k} + \Delta\boldsymbol{u}_{n+1}^{k+1}, \hat{\boldsymbol{u}}\right) = 0, \;\; \forall \hat{\boldsymbol{u}} \in \mathscr{W}_p^1\left(\Omega_0\right), \tag{23}$$

where $\boldsymbol{u}_{n+1}^{k+1} = \boldsymbol{u}_{n+1}^{k} + \Delta\boldsymbol{u}_{n+1}^{k+1}$ is the approximated iterative solution. Expanding $\mathscr{R}\left(\boldsymbol{u}_{n+1}^{k+1}, \hat{\boldsymbol{u}}\right)$ according to a *Taylor* series around $\boldsymbol{u}_{n+1}^{k}$, keeping only the first-order term, yields

$$D\mathscr{R}\left(\boldsymbol{u}_{n+1}^{k}, \hat{\boldsymbol{u}}\right)\left[\Delta\boldsymbol{u}_{n+1}^{k+1}\right] = -\mathscr{R}\left(\boldsymbol{u}_{n+1}^{k}, \hat{\boldsymbol{u}}\right), \quad \forall\hat{\boldsymbol{u}} \in \mathscr{W}_{p}^{1}\left(\Omega_0\right). \tag{24}$$

Term $D\mathscr{R}\left(\boldsymbol{u}_{n+1}^{k}, \hat{\boldsymbol{u}}\right)\left[\Delta\boldsymbol{u}_{n+1}^{k+1}\right]$ stands for the directional derivative of $\mathscr{R}$ at $\boldsymbol{u}_{n+1}^{k}$ in the direction of increment $\Delta\boldsymbol{u}_{n+1}^{k+1}$. The formal definition of this derivative is: $D\mathscr{R}\left(\boldsymbol{u}, \hat{\boldsymbol{u}}\right)\left[\Delta\boldsymbol{u}\right] = \frac{d}{d\epsilon}\mathscr{R}\left(\boldsymbol{u} + \epsilon\Delta\boldsymbol{u}, \hat{\boldsymbol{u}}\right)\big|_{\epsilon=0}$ [43, 19, 18]. Accordingly, the linearized virtual work equation at an instant t_{n+1} and iteration $k+1$ becomes [19]:

$$\int_{\Omega_0} \mathbb{M}_{n+1}^{k} : \nabla_{\boldsymbol{X}}\left(\Delta\boldsymbol{u}_{n+1}^{k+1}\right) : \nabla_{\boldsymbol{X}}\hat{\boldsymbol{u}} dV = -\mathscr{R}\left(\boldsymbol{u}_{n+1}^{k}, \hat{\boldsymbol{u}}\right), \quad \forall\hat{\boldsymbol{u}} \in \mathscr{W}_{p}^{1}\left(\Omega_0\right). \tag{25}$$

where term

$$\mathbb{M}_{n+1}^{k} \coloneqq \left.\frac{d\boldsymbol{P}}{d\boldsymbol{F}}\right|_{\boldsymbol{u}_{n+1}^{k}} \tag{26}$$

is the consistent tangent modulus calculated in terms of displacement $\boldsymbol{u}_{n+1}^{k}$. An explicit expression for $\mathbb{M}_{n+1}$ is going to be derived latter. Equation (25) has to be solved in terms of increment $\Delta\boldsymbol{u}_{n+1}^{k}$, which then provides the next iterative displacement $\boldsymbol{u}_{n+1}^{k+1} \leftarrow \boldsymbol{u}_{n+1}^{k} + \Delta\boldsymbol{u}_{n+1}^{k+1}$. Knowing the new incremental displacement, a new residual $\mathscr{R}\left(\boldsymbol{u}_{n+1}^{k+1}, \hat{\boldsymbol{u}}\right)$ is therefore computed and compared with a tolerance e_{tol}. The iterative procedure is repeated until condition $\mathscr{R}\left(\boldsymbol{u}_{n+1}^{k+1}, \hat{\boldsymbol{u}}\right) < e_{tol}$ is satisfied.

3.2 Finite element discretization

Using the finite element method to solve Eq. (25), continuum domain Ω_0 is then approximately represented by a finite number $n_e > 0$ of non-overlapping elements $\Omega_0^{(e)}$ connected by their boundary nodes: $\Omega_0 \approx {}^{h}\Omega_0 = \bigcup_{e=1}^{n_e} \Omega_0^{(e)}$. Furthermore, both displacement $\boldsymbol{u}$ and virtual displacement $\hat{\boldsymbol{u}}$ fields are approximated by their finite element counterparts:

$$\Delta\,{}^{h}\boldsymbol{u}_{n+1}^{k}\left(\boldsymbol{X}\right) = \mathbf{N}^{g}\left(\boldsymbol{X}\right)\Delta\mathbf{u}_{n+1}^{k} \;\text{ and }\; {}^{h}\hat{\boldsymbol{u}}\left(\boldsymbol{X}\right) = \mathbf{N}^{g}\left(\boldsymbol{X}\right)\hat{\mathbf{u}}, \tag{27}$$

where $\mathbf{N}^{g}$ is the global interpolation matrix, $\mathbf{u}_{n+1}^{k}$ and $\hat{\mathbf{u}}$ are the nodal displacement and virtual displacement global vectors, respectively. Gradients are approximate by: $\nabla_{\boldsymbol{X}}\boldsymbol{u}\left(\boldsymbol{X}\right) \approx \mathbf{G}^{g}\left(\boldsymbol{X}\right)\mathbf{u}$, where is the appropriate gradient of interpolation matrix $\mathbf{N}^{g}$. The stress tensor $\boldsymbol{P}$ is also replaced by a corresponding stress vector field $\mathbf{P}$. Accordingly, finite element counterpart of Eq. (25) is

$$\left(\mathbf{K}_T\right)_{n+1}^{k}\Delta\mathbf{u}_{n+1}^{k} = -R\left(\mathbf{u}_{n+1}^{k}\right), \tag{28}$$

in which $R\left(\mathbf{u}_{n+1}^{k}\right) = \left(\mathbf{f}_{int}\right)_{n+1}^{k} - \left(\mathbf{f}_{ext}\right)_{n+1}$ is the residual at iteration k. Then, the nodal displacement increment at an iteration $k+1$ and instant $t+1$ is computed by

$$\Delta\mathbf{u}_{n+1}^{k+1} = -\left[\left(\mathbf{K}_T\right)_{n+1}^{k}\right]^{-1}\left[\left(\mathbf{f}_{int}\right)_{n+1}^{k} - \left(\mathbf{f}_{ext}\right)_{n+1}\right]. \tag{29}$$

Internal $\mathbf{f}_{int}$ and external $\mathbf{f}_{ext}$ global force vectors at t_{n+1} for an iteration $k+1$ are given respectively as:

$$(\mathbf{f}_{int})_{n+1}^{k} = \int_{{}^{h}\Omega_0} (\mathbf{G}^{g})^{T} \mathbf{P}_{n+1}^{k} dV, \tag{30}$$

$$(\mathbf{f}_{ext})_{n+1} = \int_{{}^{h}\Omega_0} (\mathbf{N}^{g})^{T} \bar{\boldsymbol{b}}_{n+1} dV + \int_{{}^{h}\Gamma_0^{t}} (\mathbf{N}^{g})^{T} \bar{\boldsymbol{t}}_{n+1} dA. \tag{31}$$

Furthermore, the global stiffness tangent matrix $\mathbf{K}_T$ at t_{n+1} and iteration $k+1$ is computed according to

$$(\mathbf{K}_T)_{n+1}^{k} = \int_{{}^{h}\Omega_0} (\mathbf{G}^{g})^{T} \mathbf{M}_{n+1}^{k} \mathbf{G}^{g} dV, \tag{32}$$

where $\mathbf{M}_{n+1}^{k}$ is the matrix counterpart of the tangent modulus $\mathbb{M}_{n+1}^{k}$ defined in Eq. (26).

4 Local integration and consistent tangent modulus computation

To update the stress field $\boldsymbol{P} = \boldsymbol{P}(\boldsymbol{F}(\boldsymbol{u}))$ at each iterative step and to compute the consistent tangent modulus $\mathbb{M}$, local constitutive equations have to be integrated. For this purpose we first start by recalling the basic elements of elastic predictor-plastic corrector algorithm.

4.1 Elastic prediction and plastic correction

In the elastic prediction step, the elastic formal condition

$$\dot{\boldsymbol{F}}^{vp} = \mathbf{0} \ \text{ and } \ \dot{\alpha} = 0 \tag{33}$$

and its incremental counterpart

$$\boldsymbol{F}_{n+1}^{vp^{trial}} = \boldsymbol{F}_{n}^{vp} \ \text{ and } \ \alpha_{n+1}^{trial} = \alpha_n \tag{34}$$

hold. From these conditions, the *trial elastic state* is defined in terms of elastic deformation gradient and elastic logarithmic strain measure,

$$\boldsymbol{F}_{n+1}^{e^{trial}} = \boldsymbol{F}_{n+1} \left(\boldsymbol{F}_{n+1}^{vp^{trial}} \right)^{-1} \quad \rightarrow \quad \boldsymbol{E}_{n+1}^{e^{trial}} = \frac{1}{2} \ln \left(\boldsymbol{C}_{n+1}^{e^{trial}} \right), \tag{35}$$

with $\boldsymbol{C}_{n+1}^{e^{trial}} = \left(\boldsymbol{F}_{n+1}^{e^{trial}} \right)^{T} \boldsymbol{F}_{n+1}^{e^{trial}}$. Tensor $\boldsymbol{E}_{n+1}^{e^{trial}}$ being given, the trial-rotated *Kirchhoff* stress tensor is computed using Eq. (4): $\bar{\boldsymbol{\tau}}_{n+1}^{trial} = \bar{\boldsymbol{\tau}}_{n+1}^{trial} \left(\boldsymbol{E}_{n+1}^{e^{trial}} \right)$.

The plastic correction is required when $f\left(\bar{\boldsymbol{\tau}}_{n+1}^{trial}, A_{n+1}^{trial}\right) > 0$. The procedure adopted to perform the plastic correction refers to the return mapping algorithms, which is extensively explored in the literature. In this work, an exponential mapping is employed (see references [34, 21]). The discretization of the plastic flow $\dot{\boldsymbol{F}}^{vp} = \bar{\boldsymbol{D}}^{vp} \boldsymbol{F}^{vp}$, together with its approximation based on a backward exponential mapping, leads to

$$\boldsymbol{F}_{n+1}^{vp} = \exp\left(\Delta\lambda \boldsymbol{N}_{\bar{\boldsymbol{\tau}}_{n+1}}\right) \boldsymbol{F}_{n}^{vp}. \tag{36}$$

where $\boldsymbol{N}_{\bar{\boldsymbol{\tau}}_{n+1}} = \frac{\partial f_{n+1}}{\partial \bar{\boldsymbol{\tau}}_{n+1}} = \frac{\bar{\boldsymbol{\tau}}^D_{n+1}}{\left\|\bar{\boldsymbol{\tau}}^D_{n+1}\right\|}$. Moreover, after some manipulations Eq. (36) reduces to [34, 21]

$$\boldsymbol{E}^e_{n+1} = \boldsymbol{E}^{e^{trial}}_{n+1} - \Delta\lambda \boldsymbol{N}_{\bar{\boldsymbol{\tau}}_{n+1}}. \tag{37}$$

When the constitutive formulation is restricted to elastic and inelastic isotropy, equivalence of Eqs. (36) and (37) is exact. Otherwise, that passage is an approximation based on moderately small elastic deformation with a second-order error on elastic strains. These conditions are needed in order to obtain the relation $\boldsymbol{R}^e_{n+1} = \boldsymbol{R}^{e^{trial}}_{n+1}$, where $\boldsymbol{R}^e = \boldsymbol{F}^e \boldsymbol{U}^{e^{-1}}$ is the elastic right rotation tensor with $\boldsymbol{U}^{e^2} = \boldsymbol{F}^{e^T} \boldsymbol{F}^e$ [34, 21].

The evolution of the accumulated viscoplastic strain ϵ, introduced in Eq. (11), is approximated based on a backward *Euler* method

$$\epsilon_{n+1} = \epsilon_n + \sqrt{\frac{2}{3}}\Delta\lambda, \tag{38}$$

in which the incremental viscoplastic multiplier $\Delta\lambda$ must satisfy

$$f\left(\bar{\boldsymbol{\tau}}_{n+1}, A_{n+1}\right) = \bar{\Theta}^{-1}\left(\Delta\lambda, A_{n+1}\right), \tag{39}$$

where $\bar{\Theta}^{-1}$ is the inverse function of $\bar{\Theta}$ in terms of f_{n+1} and $\Delta\lambda$. Function $\bar{\Theta}$ is the algorithmic version of Θ given in Eq. (17).

To compute the evolution of hardening variable A from Eq. (10) together with Eq. (9), we assume that the rate $\dot{\epsilon} \approx \frac{\epsilon_{n+1}-\epsilon_n}{\Delta t}$ is constant within time step $(t_n, t_{n+1}]$. Then, Eq. (13) can be used considering t_n as the initial state and t_{n+1} as the current state, leading to

$$A_{n+1} = A_n + A_{\infty_{n+1}} c\left(\epsilon_{n+1} - \epsilon_n\right) + \left[A_{\infty_{n+1}}\left(1 + c\epsilon_n\right) - A_n\right]\left\{1 - \exp\left[-\delta\left(\epsilon_{n+1} - \epsilon_n\right)\right]\right\}, \tag{40}$$

where by virtue of Eq. (15)

$$A_{\infty_{n+1}} = \left(1 - \beta_{n+1}\right) A^{lwr}_{\infty} + \beta_{n+1} A^{up}_{\infty}, \tag{41}$$

with (see Eq. (16))

$$\beta_{n+1} = \left[\frac{1}{\Delta t}\left(\frac{\epsilon_{n+1} - \epsilon_n - \Delta t \dot{\epsilon}_{lwr}}{\dot{\epsilon}_{up} - \dot{\epsilon}_{lwr}}\right)\right]^{\xi}. \tag{42}$$

The return mapping algorithm consists therefore in determining the solution to nonlinear system of equations (37)-(42) with respect to the set of unknowns $\left\{\boldsymbol{E}^e_{n+1}, \epsilon_{n+1}, \Delta\lambda, A_{n+1}, A_{\infty_{n+1}}, \beta_{n+1}\right\}$. However, equality $\boldsymbol{N}_{\bar{\boldsymbol{\tau}}_{n+1}} = \boldsymbol{N}_{\bar{\boldsymbol{\tau}}^{trial}_{n+1}}$ can be established in the context of *von Mises* criterion stated in Eq. (6). Equations (37)-(38) thus reduce to the single scalar equation:

$$\left\|\bar{\boldsymbol{\tau}}^{D^{trial}}_{n+1}\right\| - \Delta\lambda 2\mu - \sqrt{\frac{2}{3}}\left(\sigma_y + A_{n+1}\right) = \bar{\Theta}^{-1}\left(\Delta\lambda, A_{n+1}\right), \tag{43}$$

with unknowns $\Delta\lambda$ and A_{n+1}. Furthermore, inserting Eq. (38) into Eq. (40) yields

$$A_{n+1} = A_n + A_{\infty_{n+1}} c\sqrt{\frac{2}{3}}\Delta\lambda + \left[A_{\infty_{n+1}}\left(1 + c\epsilon_n\right) - A_n\right]\left[1 - \exp\left(-\delta\sqrt{\frac{2}{3}}\Delta\lambda\right)\right], \quad (44)$$

while substituting Eqs. (38) and (42) into Eq. (41) gives

$$A_{\infty_{n+1}} = A_\infty^{lwr} + \left[\frac{1}{\Delta t}\left(\frac{\sqrt{\frac{2}{3}}\Delta\lambda - \Delta t\dot{\epsilon}_{lwr}}{\dot{\epsilon}_{up} - \dot{\epsilon}_{lwr}}\right)\right]^{\xi}\left(A_\infty^{up} - A_\infty^{lwr}\right). \quad (45)$$

Then, the reduced return mapping algorithm consists in solving Eqs. (43)-(45) with respect to $\Delta\lambda$, A_{n+1} and $A_{\infty_{n+1}}$. Derivatives of Eqs. (43)-(45) with respect to unknowns $\left\{\Delta\lambda, A_{n+1}, A_{\infty_{n+1}}\right\}$, required into nonlinear problem solution, are given in A.

4.2 Consistent tangent modulus

Consistent tangent modulus introduced in Eq. (26) can be given in components according to

$$M_{ijkl_{n+1}} = \left(\frac{\partial\tau_{ip}}{\partial F_{kl}}F_{jp}^{-1} - \tau_{ip}F_{jk}^{-1}F_{lp}^{-1}\right)_{n+1}. \quad (46)$$

Computation of $\mathbb{M}_{n+1}$ requires the derivative calculation of $\boldsymbol{\tau}$ with respect to $\boldsymbol{F}$ at t_{n+1}. However, expressing $\boldsymbol{\tau}$ as a function of the rotated *Kirchhoff* stress tensor $\bar{\boldsymbol{\tau}}$ provides an alternative way to compute this derivative,

$$\tilde{\mathbb{D}}_{n+1} = \frac{\partial\bar{\boldsymbol{\tau}}_{n+1}}{\partial\boldsymbol{F}_{n+1}} = \mathbb{D}_{n+1} : \mathbb{P}_{n+1} : \mathbb{Q}_{n+1}, \quad (47)$$

since $\bar{\boldsymbol{\tau}}_{n+1}$ is a function of input variables $\boldsymbol{E}_{n+1}^{e^{trial}}$ and α_n. In the above equation, $\mathbb{D}_{n+1} = \frac{\partial\bar{\boldsymbol{\tau}}_{n+1}}{\partial\boldsymbol{E}_{n+1}^{e^{trial}}}$, $\mathbb{P}_{n+1} = \frac{\partial\boldsymbol{E}_{n+1}^{e^{trial}}}{\partial\boldsymbol{C}_{n+1}^{e^{trial}}}$ and $\mathbb{Q}_{n+1} = \frac{\partial\boldsymbol{C}_{n+1}^{e^{trial}}}{\partial\boldsymbol{F}_{n+1}}$. Observing that $\boldsymbol{C}_{n+1}^{e^{trial}} = \left(\boldsymbol{F}_{n+1}^{e^{trial}}\right)^T\boldsymbol{F}_{n+1}^{e^{trial}}$, the components of the fourth-order tensor $\mathbb{Q}_{n+1}$ read

$$Q_{ijkl_{n+1}} = F_{li_n}^{vp^{-1}}F_{kj_{n+1}}^{e^{trial}} + F_{ki_{n+1}}^{e^{trial}}F_{lj_n}^{vp^{-1}}. \quad (48)$$

The fourth-order tensor $\mathbb{P}_{n+1}$ is computed as

$$\mathbb{P}_{n+1} = \frac{\partial}{\partial\boldsymbol{C}_{n+1}^{e^{trial}}}\ln\left(\boldsymbol{U}_{n+1}^{e^{trial}}\right) = \frac{1}{2}\frac{\partial}{\partial\boldsymbol{C}_{n+1}^{e^{trial}}}\ln\left(\boldsymbol{C}_{n+1}^{e^{trial}}\right). \quad (49)$$

The terms $\mathbb{P}_{n+1}$ and $\mathbb{Q}_{n+1}$ are geometrical quantities related to finite strains while the tangent operator $\mathbb{D}_{n+1}$ is the unique term of $\tilde{\mathbb{D}}_{n+1}$ that depends on material response. In the elastic range, $\mathbb{D}_{n+1}$ turns to be coincident with the elastic stiffness $\mathbb{D}^e$, while it becomes the elastic-viscoplastic tangent operator

$$\mathbb{D}_{n+1}^{vp} = \frac{\partial\bar{\boldsymbol{\tau}}_{n+1}}{\partial\boldsymbol{E}_{n+1}^{e^{trial}}} \quad (50)$$

in the inelastic range. Evaluation of $\mathbb{D}^{vp}_{n+1}$ is obtained from linearization of Eqs. (37), (39), (45) and (44), what yields (see B)

$$\mathbb{D}^{vp}_{n+1} = \frac{\partial \bar{\boldsymbol{\tau}}_{n+1}}{\partial \boldsymbol{E}^{e^{trial}}_{n+1}} = \left(\mathbb{D}^{e^{-1}} + \Delta\lambda \frac{\partial \boldsymbol{N}_{\bar{\boldsymbol{\tau}}_{n+1}}}{\partial \bar{\boldsymbol{\tau}}_{n+1}} + \frac{1}{\chi} \boldsymbol{N}_{\bar{\boldsymbol{\tau}}_{n+1}} \otimes \boldsymbol{N}_{\bar{\boldsymbol{\tau}}_{n+1}} \right)^{-1}, \tag{51}$$

where

$$N_{A_{n+1}} = \frac{\partial f_{n+1}}{\partial A_{n+1}}, \tag{52}$$

$$\chi = \left[\frac{\partial \bar{\Theta}^{-1}}{\partial \Delta\lambda} + \left(\frac{\partial \bar{\Theta}^{-1}}{\partial A_{n+1}} - N_{A_{n+1}} \right) \Lambda \right], \tag{53}$$

$$\begin{aligned} \Lambda \;=\; & \left[(1 + c\epsilon_n)(1 - \varphi) + c\sqrt{\frac{2}{3}}\Delta\lambda \right] \omega + \dots \\ & \dots + \sqrt{\frac{2}{3}} \left\{ \delta \left[A_{\infty_{n+1}} (1 + c\epsilon_n) - A_n \right] \varphi + A_{\infty_{n+1}} c \right\}, \end{aligned} \tag{54}$$

$$\omega = \sqrt{\frac{2}{3}} \frac{\xi}{\Delta t} \left(\frac{A^{up}_{\infty} - A^{lwr}_{\infty}}{\dot{\epsilon}_{up} - \dot{\epsilon}_{lwr}} \right) \left[\frac{1}{\Delta t} \left(\frac{\sqrt{\frac{2}{3}}\Delta\lambda - \Delta t \dot{\epsilon}_{lwr}}{\dot{\epsilon}_{up} - \dot{\epsilon}_{lwr}} \right) \right]^{\xi - 1}, \tag{55}$$

$$\varphi = \exp\left(-\delta \sqrt{\frac{2}{3}} \Delta\lambda \right). \tag{56}$$

5 Numerical results and discussion

Aiming to assess the capabilities of the present constitutive model in accounting for strain hardening, strain rate hardening and viscous effects, the numerical procedure described in Section 4 is first applied to analyze the local material response subjected to uniaxial tension/compression loading. The latter is described by prescribing the value of axial strain E_{11} and associated strain rate $\bar{D}_{11}$. The material is elastic-viscoplastic and the corresponding material parameters to be used are given in Tab. 1. These parameters were obtained in a previous work [26] considering experimental data for an annealed OFHC copper available in the literature [3, 7, 35]. Classical relationships relate the *Young* modulus E and *Poisson* ratio ν appearing in Tab. 1 with elastic coefficients μ and κ of Eq. (4) through $\mu = \frac{E}{2(1+\nu)}$ and $\kappa = \frac{E}{3(1-2\nu)}$. We emphasize that the elastic part of strain is expected to be infinitesimal since the ratio $\frac{\sigma_y + A}{E}$ is very small when compared to unity. Furthermore, it should be kept in mind that the *Perić* viscoplastic function is considered throughout the paper, see Eqs. (17)-(19).

Table 1: Material properties and model parameters associated with annealed OFHC copper [26].

E [GPa]	ν [–]	σ_y [MPa]	δ [–]	c [–]	A_∞^{lwr} [MPa]	A_∞^{up} [MPa]	$\dot{\epsilon}_{lwr}$ [s^{-1}]	$\dot{\epsilon}_{up}$ [s^{-1}]	ξ [–]	ϑ [s]	m [–]
112	0.33	35	6.46	0.42	233	420	10^{-4}	10^4	3.16	1.2×10^3	105

5.1 Decremental strain rate test

Strain rate hardening (or strain rate history) effects can be demonstrated from decremental strain rate testing. In this case, the material is subjected to a monotonic loading with a given initial strain rate $\bar{D}_{11_1}$ which is then abruptly decreased to a value $\bar{D}_{11_2}$. The phenomenon is evidenced when the decremental response is compared to those obtained during a monotonic loading under a constant strain rate $\bar{D}_{11} = \bar{D}_{11_2}$ during overall deformation process. For this purpose the present analysis will include two load conditions (employed in experiments of [3]):

- Q.S.: *quasi*-static test. Material is subjected to a total strain equal to 92% imposed very slowly with $\bar{D}_{11} = 4 \times 10^{-4}\,\mathrm{s}^{-1}$;
- D.T.: decremental strain rate test. Material is subjected to at a high strain rate of $\bar{D}_{11_1} = 6 \times 10^3\,\mathrm{s}^{-1}$ until a partial strain of 32% is reached, then the strain rate is abruptly changed to a lower value $\bar{D}_{11_2} = 4 \times 10^{-4}\,\mathrm{s}^{-1}$ while strain reaches 79%.

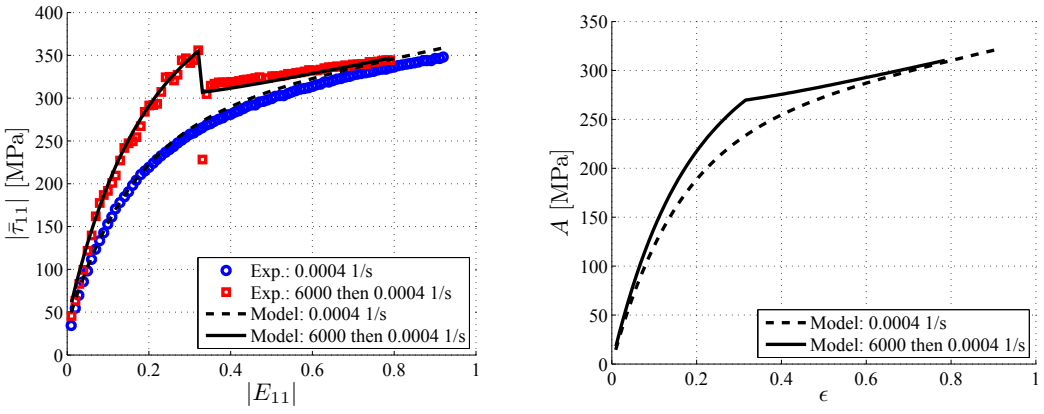

(a) (b)

Figure 1: Decremental strain rate test results: (a) Model-predicted stress-strain curves compared with experimental data of [3]; (b) Stress hardening vs. accumulated viscoplastic strain curves.

Numerical analyzes were performed considering a local convergence tolerance equal to 10^{-6}, 92 time steps[3] for *Q.S.* simulation and 78 for *D.T.* case. The numerical results are depicted in Figs. 1(a) and (b) showing the effects of strain rate history on the material response. Figure 1(a) shows the stress-strain curves for *Q.S.* and *D.T.* results are

[3]Numbers of time steps are equal to number of experimental points.

compared with experiments of [3], where a good agreement between predicted and experimental data is observed. When the strain rate changes abruptly from $\bar{D}_{11_1} = 6 \times 10^3\,\mathrm{s}^{-1}$ to $\bar{D}_{11_2} = 4 \times 10^{-4}\,\mathrm{s}^{-1}$, an abrupt change in flow stress is observed. It is due to instantaneous strain rate sensitivity related to viscous mechanisms, while no jump is observed in hardening response as illustrated by Fig. 1(b). This behavior feature could be expected, since parameter A is related to current microstructural configuration, which does not undergo an instantaneous change by abruptly shifting strain rate (see reference [1]). Moreover, *Q.S.* curves should only be recovered asymptotically by both stress and hardening responses of *D.T.* simulation. This is attributed to the fact that the flow stress does not depend only on instantaneous values of strain rate, but also on strain rate history. In other words, a higher previous strain rate induces a larger hardening when compared to a lower strain rate imposed during the whole deformation process, what can be physically related to the rate-dependence of dislocation storage [1, 2, 44, 45]. This rate-sensitivity is captured by the present model through the rate dependence attributed to saturation hardening A_∞ (see Eq. (15)).

5.2 Rate-dependence and stress relaxation

The current material strength induced by previous deformation history can also be characterized from stress relaxation testing, where the obtained equilibrium state reflects the current microstructural configuration. Thereby, the strain rate history effects on material state can be evaluated by varying the loading strain rate preceding stress relaxation, and thus observing the associated equilibrium stress states that are reached asymptotically. A constitutive model capable of accounting for strain rate history effects should theoretically be able to predict the distinct equilibrium stress states reached after different previous loading strain rates. For this purpose, numerical simulations of stress relaxation tests are undertaken using the proposed elastic-viscoplastic formulation.

Table 2: Loading strain rates of stress relaxation testing.

	Q.S.	case *R1*	case *R2*	case *R3*
$\bar{D}_{11}$ [s^{-1}]	4×10^{-4}	10^3	6×10^3	9×10^3

The numerical analyzes are carried out prescribing a total strain equal to 100% at different strain rates (see Tab. 2) and then keeping it constant along time. The material properties are those given in Tab. 1. All analyzes were performed considering 200 time steps and a local convergence tolerance equal to 10^{-6}. The stress-strain curves obtained for loading and stress relaxation simulations are shown in Fig. 2(a). In this figure, cases *Q.S.*, *R2* and *R3* are compared with experiments showing a good agreement. As expected, the flow stress is an increasing function of strain rate. This effect could readily be predicted by a conventional viscoplastic model that accounts only for instantaneous rate-sensitivity. However, the proposed constitutive model is also capable to predict the hardening rate-sensitivity, since the hardening A should be a direct consequence of the

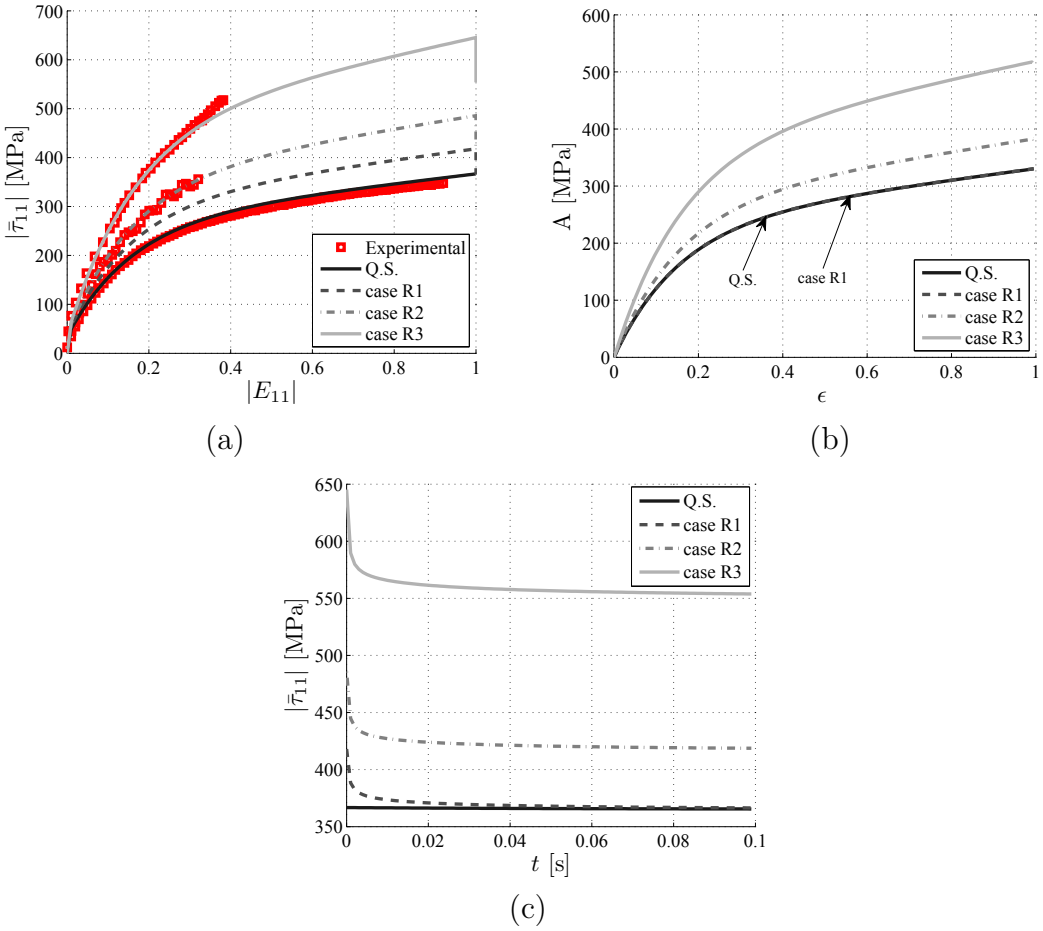

Figure 2: (a) Strain rate effects on stress-strain curves: comparison of model prediction and experiments of [3] (*Q.S.* and *R2*) and of [35] (*R3*); (b) Strain rate history effect on hardening curves; (c) Strain rate history effect on stress relaxation.

current microstructure, which in turn is affected by the whole plastic strain and strain rate history and not only by their current values.

In the proposed model, the hardening variable A increases with rate $\dot{\epsilon}$, as emphasized in Fig. 2(b). But, the strain rate influence on hardening becomes significant only for strain rates greater than $10^3\,\mathrm{s}^{-1}$. That is, up to a strain rate of $10^3\,\mathrm{s}^{-1}$ (cases *Q.S.* and *R1*) hardening responses are practically overwritten and for strain rates exceeding $10^3\,\mathrm{s}^{-1}$ (cases *R2* and *R3*) the effect of previous strain rate history upon A becomes significant. The rate dependence of hardening variable A can also be clearly evidenced in Fig. 2(c), where the relaxation response tends toward an asymptotic equilibrium stress state, which is given by the non-viscous stress $(\sigma_y + A)$ associated with each previous loading strain rate. In this figure, we observe that *R1* curve reaches the *Q.S.* response asymptotically, what demonstrates that the difference between cases *Q.S.* and *R1* observed in Fig. 2(a) is mainly due to viscous effects. On the other hand, the equilibrium stress state $(\sigma_y + A)$ is significantly increased by strain rate for values exceeding $10^3\,\mathrm{s}^{-1}$. Note that the reference

time $t = 0$ in Fig. 2(c) corresponds to the instant at which the stress relaxation starts.

5.3 Billet upsetting simulation

In order to evaluate the whole numerical framework (local constitutive integration and finite element solution), a billet upsetting simulation is carried out in the sequel. Numerical results are compared with analytical solution, which was derived in work [26] for uniaxial compression test,

$$|\bar{\tau}_{11}| = (\sigma_y + A)\left(1 + \sqrt{\frac{3}{2}}\vartheta\dot{\epsilon}\right)^{\frac{1}{m}}, \tag{57}$$

where $|\bar{\tau}_{11}|$ is the absolute value of axial rotated *Kirchhoff* stress. The analyzes aim to demonstrate the strain rate effects on plastic fields of a non-homogeneous deformation process. Furthermore, to assess numerical efficiency and robustness convergence studies are performed. Convergence criterion is the number of iterations (n_{iter}) to reach the admissible error given by $\|\boldsymbol{r}_{n+1}\|_{\infty}^{adm} = 10^{-6}$. The residue vector is the classical one used into finite element framework, $\boldsymbol{r} = \boldsymbol{f}^{ext} - \boldsymbol{f}^{int}$, in which $\boldsymbol{f}^{ext}$ and $\boldsymbol{f}^{int}$ are the external and internal finite element force vectors, respectively.

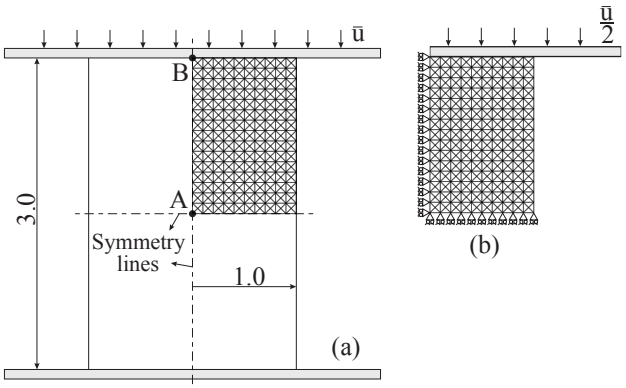

Figure 3: (a) Axisymmetric billet upsetting model (dimensions are in mm); (b) Finite element mesh and boundary conditions for a quarter of workpiece.

Figure 3 schematically presents the axisymmetric model considered for analysis, where upper and lower gray regions represent rigid platens. Finite element discretization consists of 600 quadratic triangular elements (1251 nodes). Material parameters are also those of Tab. 1. The contact formulation is based on *Signorini* condition and friction is modeled by regularized *Coulomb* model with a friction coefficient of $f_c = 0.1$ and regularization parameter $\epsilon_T = 10^{-4}$. The *Augmented Lagrangian* algorithm [46, 47] is employed to impose the contact, and penalty parameter associated with the impenetrability condition is set as $\epsilon_v = 10^{-7}$. The main focus of the present simulation is to analyze the structural response in frictional compression test. However, the simulation with $f_c = 0$ shall also be performed and corresponding predictions compared to analytical results derived for

frictionless case. Starting from $\bar{u}\,(t=0)=0$, the prescribed displacement takes the form [26]:

$$\bar{u}\,(t) = l_0\,[1-\exp\,(Kt)]\,, \tag{58}$$

which would correspond in a frictionless problem to a homogeneous axial strain rate of $-\bar{D}_{11} = K > 0$. In Eq. (58) $l_0 = 3\,\text{mm}$ is the specimen initial length. A total prescribed displacement $\bar{u}_{total} = 1.0\,\text{mm}$ is applied and maintained in 100 equal time steps (50 for loading stage and 50 for stress relaxation phase). Considering different values of K according to Tab. 2, the loading process is defined as follows:

$$\bar{u}\,(t) = \begin{cases} l_0\,[1-\exp\,(Kt)] & 0 \le t \le T \\ \bar{u}_{total} & T \le t < \infty \end{cases}\,, \tag{59}$$

with $\bar{u}_{total} = l_0\,[1-\exp\,(KT)]$ being the total prescribed displacement reached at an instant $t = T$. For $t \ge T$, the applied displacement is maintained constant along time in order to investigate the structural response during stress relaxation test. Considering the friction case, the prescribed displacement $\bar{u}_{total} = 1.0\,\text{mm}$ induces a non-homogeneous strain field in the specimen whose maximum magnitude is in all cases lower than 55%. The limitation to this strain level has been deliberately adopted to avoid numerical difficulties, thus focusing on the constitutive effects of numerical modeling. For example, the present numerical strategy does not prevent volumetric locking, and in this case it expected that for strains higher than 0.55 this numerical issue can become significant.

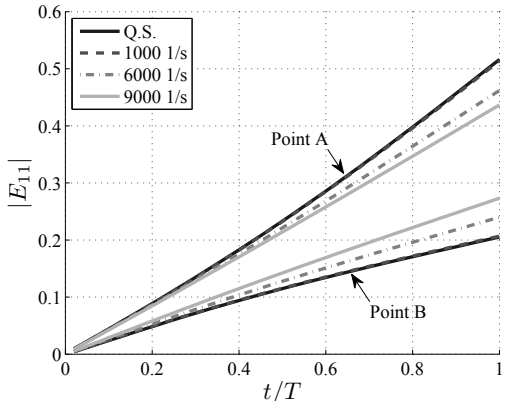

Figure 4: Influence of loading rate parameter K on axial strain of point A and point B (friction cases).

As mentioned early, friction conditions along loaded faces induce a heterogeneous strain field in the specimen. This aspect will be characterized considering two distinct points A and B of the discretized workpiece, see Fig. 3(a). The loading rate influence on axial strain history of points A and B is shown in Fig. 4, that is, the influence of loading rate parameter K on axial strain response vs. normalized time $\frac{t}{T}$. Due to friction effects, point B undergoes smaller strains than point A, since this phenomenon restricts the radial displacement at platen/specimen interface. However, increasing K leads to a decrease in axial strain of point A, while it induces an increase in axial strain of B.

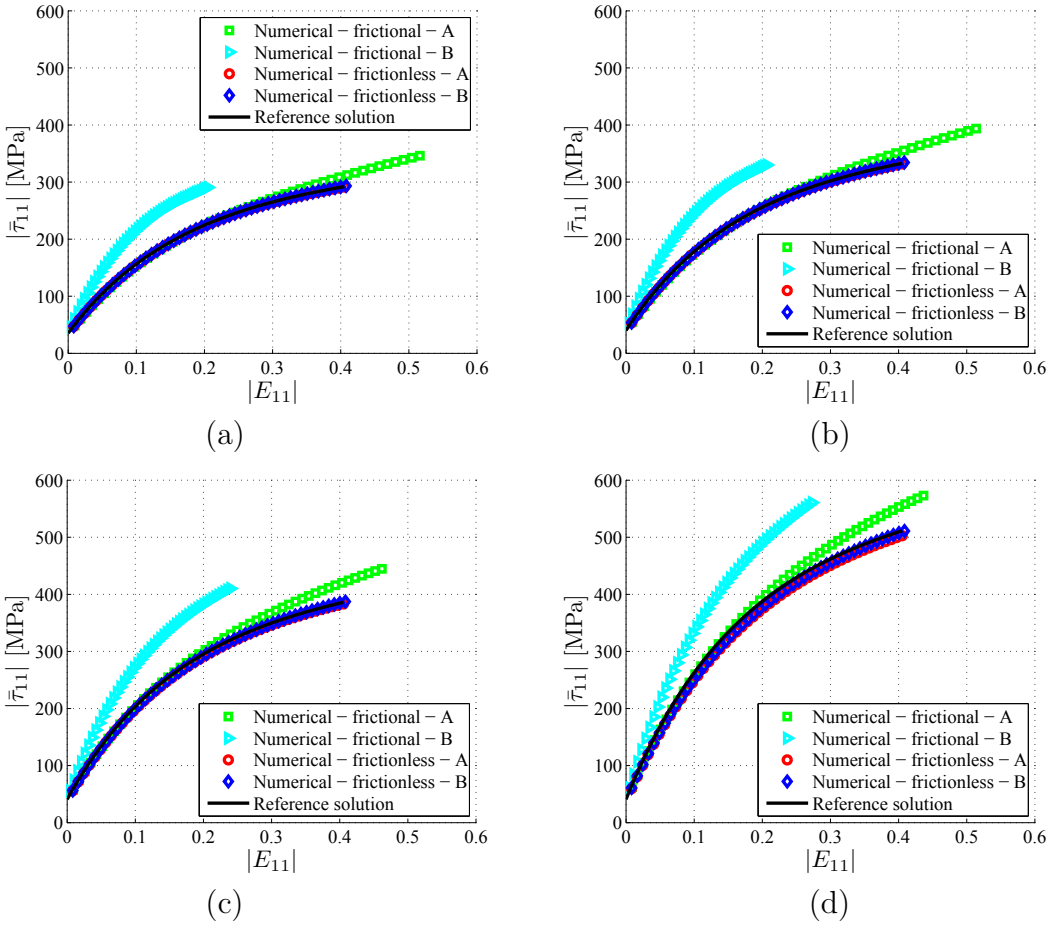

Figure 5: Axial stress vs. strain curves: (a) *Quasi*-static case, $K = 4 \times 10^{-4}\,\mathrm{s}^{-1}$; (b) $K = 10^{3}\,\mathrm{s}^{-1}$; (c) $K = 6 \times 10^{3}\,\mathrm{s}^{-1}$; (d) $K = 9 \times 10^{3}\,\mathrm{s}^{-1}$.

Figures 5(a)-(d) display, for different values of K, the axial rotated *Kirchhoff* stress vs. strain curves of points A and B. In addition to results obtained from numerical simulations of frictional compression test, these figures also show the numerical predictions for frictionless situation as well as for the rigid-viscoplastic analytical solution given in Eq. (57). Note that frictionless numerical predictions are very close to analytical reference solution. In friction case, the response of point A remains close to that obtained in frictionless compression (reference situation) until a strain of about 20%. Beyond this strain level, the response in friction case begins to deviate from this reference situation. In contrast, due to confined strain state, stress triaxiality appears in vicinity of point B right after the loading process has started, leading to lower strain and higher stress levels than at point A.

Comparisons for different values of K of axial rotated *Kirchhoff* stress vs. logarithmic strain curves are shown in Figs. 6(a) and (b) for frictional compression test. This comparisons indicate that increasing the value of K induces higher absolute stress levels in the specimen. However, the maximum strain level decreases with K at point A, while it

exhibits opposite trend at point B.

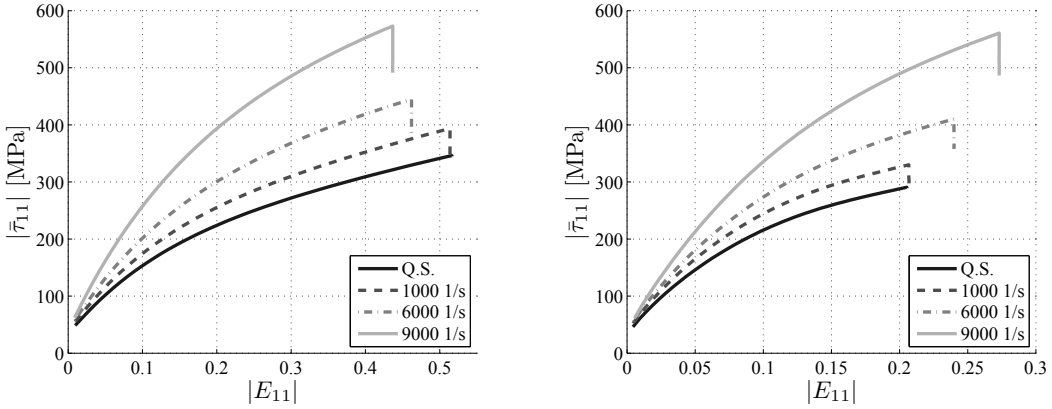

Figure 6: Influence of loading rate parameter K on axial stress vs. strain curves (friction cases): (a) Point A; (b) Point B.

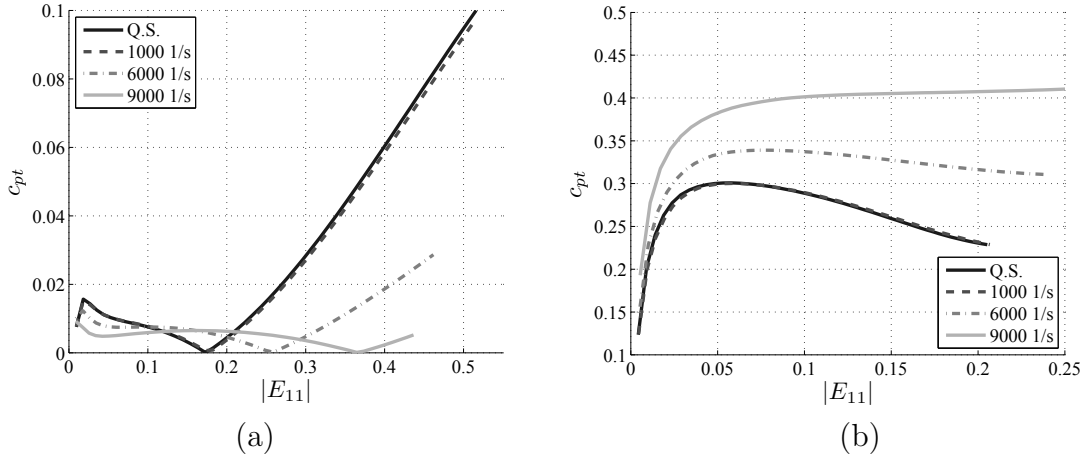

Figure 7: Influence of loading rate parameter K on pressure transmission coefficient $c_{pt} = \frac{\bar{\tau}_{22}}{\bar{\tau}_{11}}$ vs. strain curves (friction cases): (a) Point A; (b) Point B.

Stress triaxiality effects are illustrated in Figs. 7(a) and 7(b), where the pressure transmission coefficients[4] $c_{pt} = \frac{\bar{\tau}_{22}}{\bar{\tau}_{11}}$ at points A and B are plotted against the axial strain. Scalars $\bar{\tau}_{11}$ and $\bar{\tau}_{22}$ refer to axial and radial rotated *Kirchhoff* stresses, respectively. In accordance with observations related to Figs. 5, it is first observed that ratio c_{pt} at point A remains very small for strain lower than 20%, and then increases continuously with the strain level (Fig. 7(a)). In contrast, ratio c_{pt} at point B increases rapidly with strain in the small range (until $\approx 5\%$), followed by a moderate decreasing with strain level (Fig. 7(b)).

[4]It is worth to recall that in an axisymmetric deformation the value $c_{pt} = 0$ indicates an axial stress

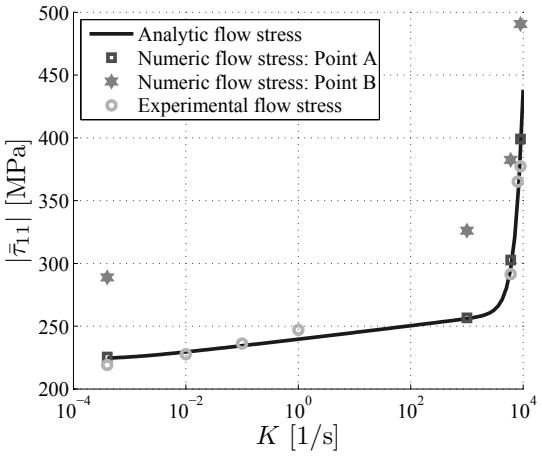

Figure 8: Influence of loading rate parameter K on flow stress of Point A and Point B, for a given absolute strain of 0.2 (friction cases). Analytical solution is taken from Eq. (57), considering a frictionless rigid-viscoplastic case. Experimental data were taken from references [3, 7, 35] considering an annealed OFHC copper (see also reference [26]).

Concerning the strain rate sensitivity, in Fig. 8 the influence of loading rate parameter K on flow stress response can be realized, considering a given absolute strain level of 0.2. In this figure an upturn in the rate sensitivity is observed for values of K greater than $10^3\,\mathrm{s}^{-1}$. As discussed by some authors (see for instance [48, 8, 26]) this sudden upturn behavior is a result of the strain rate hardening observed e.g. in FCC metals as copper and aluminum. Notice that the stress response of point A is very close to the frictionless rigid-viscoplastic analytical solution given in Eq. (57) and to the experimental data related to annealed OFHC copper, see [3, 7, 35]. However, in contrast to point A, due to confined strain state and then to higher stress triaxiality, point B presents a higher absolute stress level for the same given total strain of 0.2.

The overall behavior of structure may be characterized by means of the evolution of resultant vertical force applied to specimen with respect to prescribed displacement. Figures 9(a)-(d) show the results obtained from numerical simulations as well as analytical solution for frictionless compression obtained from stress solution of Eq. (57)

$$|f_1| = \frac{V_0}{l}\,|\bar{\tau}_{11}|\,, \tag{60}$$

where $|f_1|$ is the resultant applied force, V_0 is the initial volume and l is the current length of workpiece. The numerical frictionless results are very close to analytical reference solutions. However, slight effects of friction are observed as prescribed displacement is increasing. It is emphasized that the whole results should be interpreted keeping in mind that the considered value of friction coefficient is rather small ($f_c = 0.1$). Regarding the influence of strain rate parameter K, Figs. 10(a) and (b) corroborate, as expected, that higher forces are needed to impose a given displacement when the loading rate K increases.

state and $c_{pt} = 1$ a hydrostatic stress state.

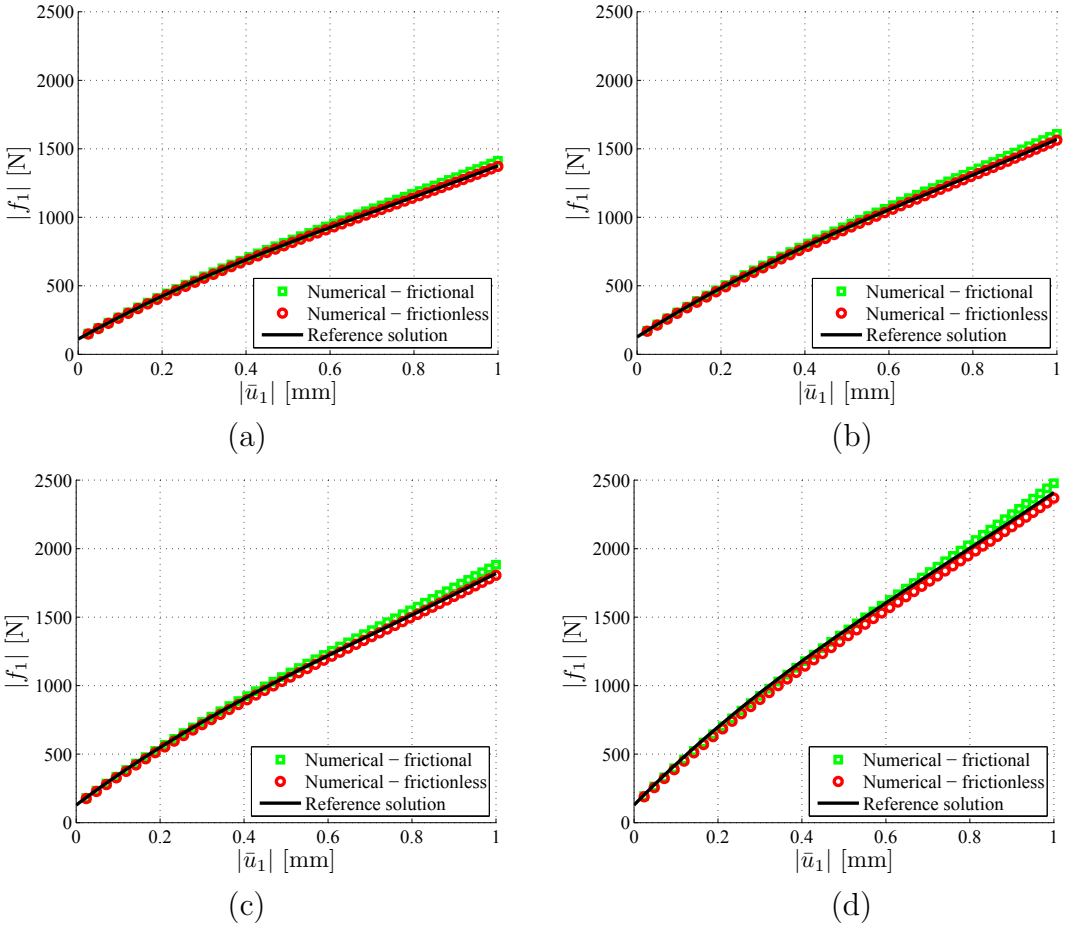

Figure 9: Applied force vs. applied displacement curves: (a) *Quasi*-static case, $K = 4 \times 10^{-4}\,\mathrm{s}^{-1}$; (b) $K = 10^3\,\mathrm{s}^{-1}$; (c) $K = 6 \times 10^3\,\mathrm{s}^{-1}$; (d) $K = 9 \times 10^3\,\mathrm{s}^{-1}$. Notice that the reference solution is for rigid-viscoplastic case, see Eq. (57), while the FE solution is for elastic-viscoplastic one.

The capability of the proposed constitutive model to capture the effects of strain rate on stress response has been illustrated in Figs. 6, which indicate that axial stress-strain curves are significantly affected by the value of imposed loading rate K. At strain rates until $10^3\,\mathrm{s}^{-1}$ the rate dependence is mainly due to viscous effects, and for strain rates exceeding $10^3\,\mathrm{s}^{-1}$ proposed model accounts for the dependence of hardening with respect to strain rate (see for instance [26]). The effects of strain rate on the material hardening response are clearly evidenced in Figs. 11(a) and (b) in frictional compression test with $f_c = 0.1$. These figures emphasize how increasing the value of K induces, for a given accumulated viscoplastic strain, a larger material hardening. However, note that the curves related to cases *Q.S.* and $K = 10^3\,\mathrm{s}^{-1}$ are practically overwritten, what clearly shows that for strain rates $< 10^3\,\mathrm{s}^{-1}$ the proposed model predicts a small strain rate influence on hardening response.

The analysis performed during loading phase ($t \leq T$) suggests that, due to rate sensitivity of material hardening, significant effects of strain rate on flow stress rise when

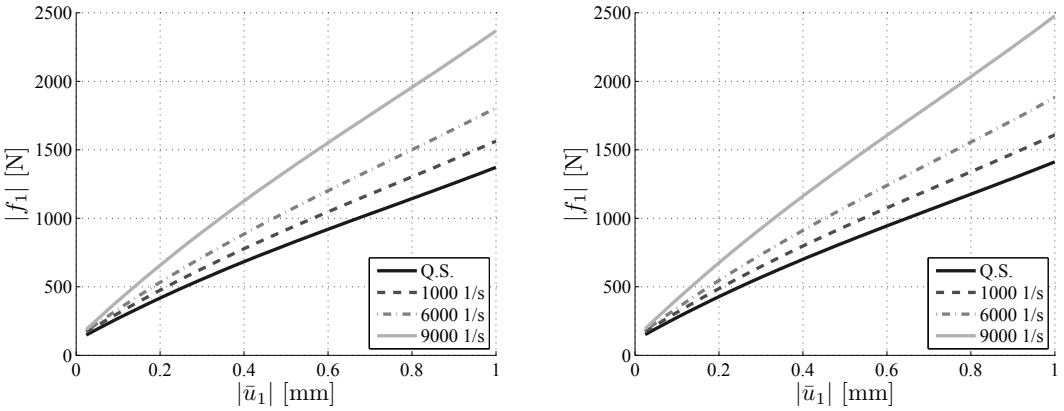

Figure 10: Influence of loading rate parameter K on applied force vs. applied displacement curves: (a) Frictionless; (b) Frictional cases.

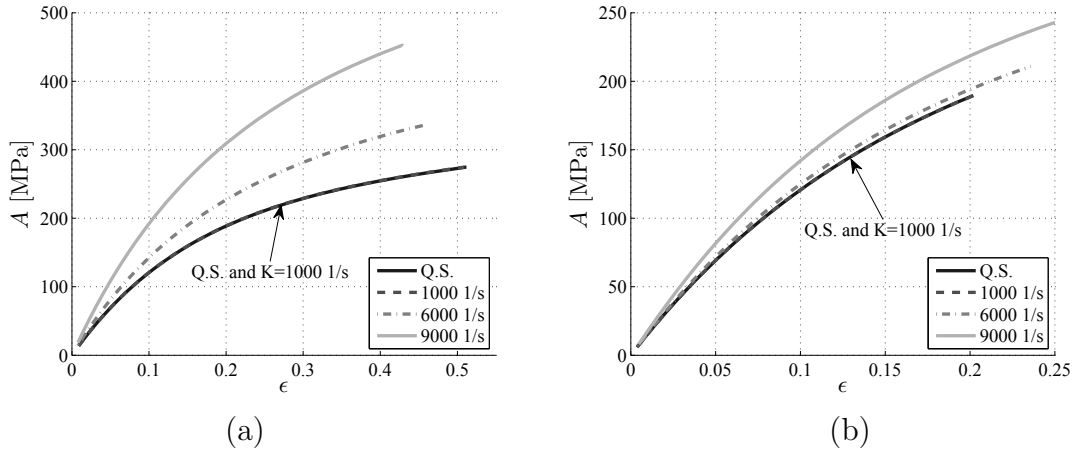

Figure 11: Influence of loading rate parameter K on stress hardening vs. accumulated viscoplastic strain (friction cases): (a) Point A; (b) Point B.

$K > 10^3\,\mathrm{s}^{-1}$. This feature is also corroborated in the relaxation phase imposed to specimen. Figures 12(a) and (b) present the stress relaxation curves of points A and B, i.e., evolution of axial rotated *Kirchhoff* stress vs. time t. It is observed from these figures that the equilibrium stress state (asymptotic stress state) reached after relaxation process is generally sensitive to strain rate history. However, since equilibrium stress quantity is a direct consequence of material hardening, as commented early, the strain rate influence on relaxed state becomes significant only for loading rates $K > 10^3\,\mathrm{s}^{-1}$. Consequently, the case with $K = 10^3\,\mathrm{s}^{-1}$ tends asymptotically to the *Q.S.* curve. The reference time $t = 0$ in Fig. 12 corresponds to instant (T) at which the stress relaxation starts.

An alternative way to illustrate the strain rate history effects on specimen response consists of visualizing the contours of *von Mises* equivalent stress, as displayed in Figs. 13(a)-(d). Two particular instants are considered for each value of K, namely at the

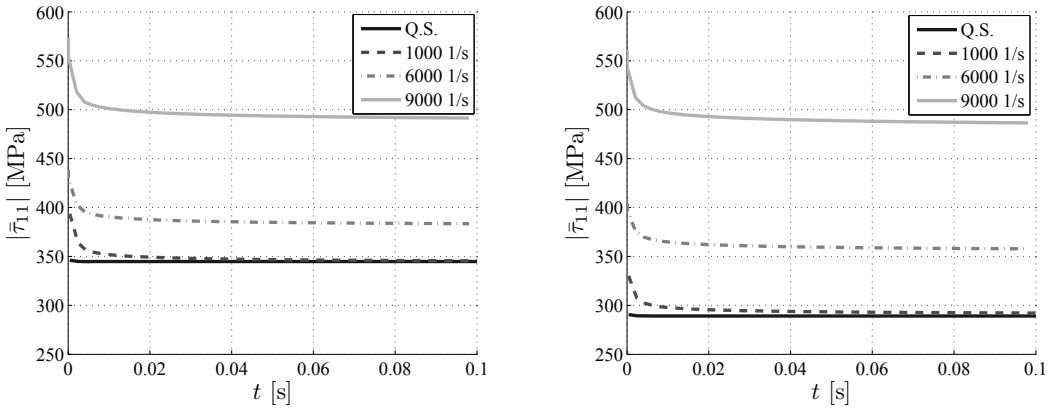

Figure 12: Influence of loading rate parameter K on stress relaxation (friction cases): (a) Point A; (b) Point B.

onset of stress relaxation ($t = T$) and at the relaxed state. Once again, these figures confirm the existence of a value of loading rate beyond which strain rate history effects prove significant. As expected, no noticeable change is observed between the "before relaxation" and "after relaxation" states for the *quasi*-static case. In contrast, significant changes between the "before relaxation" and "after relaxation" states are observed for the high strain rate cases ($K \geq 10^3\,\mathrm{s}^{-1}$), what is due to instantaneous viscous effects. Furthermore, comparison of all "after relaxation" states indicates that the $K = 10^3\,\mathrm{s}^{-1}$ case relaxes to a state close to the *quasi*-static one. On the other hand, higher values of K leads to higher absolute values of equilibrium stress fields.

The performance of numerical procedure is assessed by means of convergence analyzes in both *quasi*-static and high strain rate ($K = 9 \times 10^3\,\mathrm{s}^{-1}$) cases. The results are summarized in Tab. 3 for $\frac{t}{T} \in \{0.02, 0.2, 0.5, 1.0\}$ considering frictionless ($f_c = 0$) and frictional ($f_c = 0.1$) compression. In this table term AL_i stands for the number of iterations to reach convergence in the *Augmented Lagrangian* algorithm employed to solve contact problem [46, 47] and n_{iter} for the number of iterations to reach finite element equilibrium ($\|\boldsymbol{r}_{n+1}\|_\infty \leq 10^{-6}$). The end of loading phase ($t = T$) in *Q.S.* case correspond to the higher required iterations for numerical convergence ($n_{iter} = 15$). Table 3 also indicates that convergence is enhanced with higher loading rate K.

Convergence curves are displayed in Figs. 14(a) and (b) for simulations considering smooth and frictional contact in the *quasi*-static and high strain rate ($K = 9 \times 10^3\,\mathrm{s}^{-1}$) cases. Two particular instants were examined, namely $\frac{t}{T} = 0.02$ and $\frac{t}{T} = 1.0$. Figure 14(a) shows that there is no significant difference between the *quasi*-static and high strain rate cases for frictionless compression simulations. On the other hand, it is observed in Fig. 14(b) that the convergence is significantly improved when imposing a higher strain rate in the case of frictional compression test. As a matter of fact, the number of iterations for convergence drops from 50 to 5 at instant $\frac{t}{T} = 1.0$ and iteration $AL_i = 2$ of *Augmented Lagrangian* algorithm. Furthermore, as can be seen in Tab. 3, the *Augmented Lagrangian* algorithm took 3 steps to converge in the *quasi*-static frictional problem. The *quasi*-static

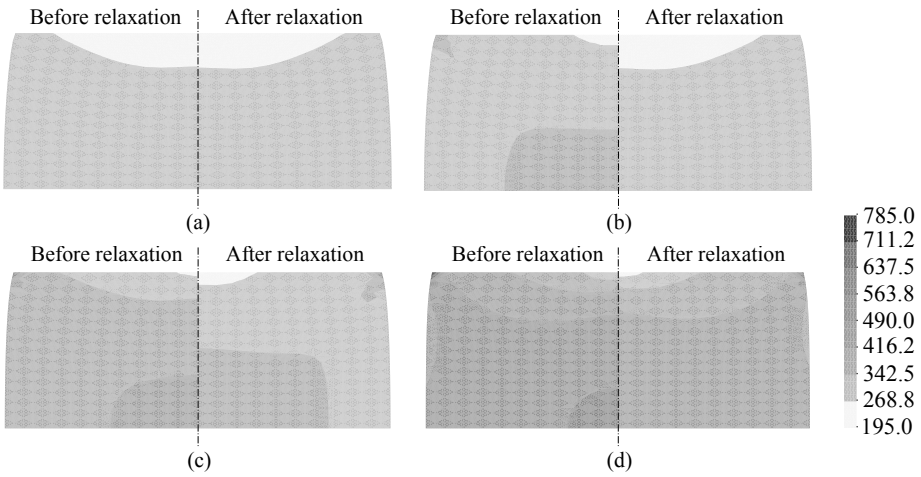

Figure 13: Contours of *von Mises* equivalent stress [MPa], before stress relaxation ($t = T$) and after stress relaxation: (a) *Quasi*-static case, $K = 4 \times 10^{-4}\,\mathrm{s}^{-1}$; (b) $K = 10^{3}\,\mathrm{s}^{-1}$; (c) $K = 6 \times 10^{3}\,\mathrm{s}^{-1}$; (d) $K = 9 \times 10^{3}\,\mathrm{s}^{-1}$.

simulation has a worse global convergence because, in addition to the trial elastic state being far from the current solution, in this case a higher time increment Δt is obtained, what can give an ill-conditioned tangent operator $\mathbb{D}^{vp}$. See for instance Eqs. (51)-(55), as well as Eqs. (70) and (71).

Table 3: Number of iterations required for convergence of frictional contact algorithm.

$\frac{t}{T}$ - (step number)	AL_i	*Quasi*-static		$K = 9 \times 10^{3}\,\mathrm{s}^{-1}$	
		n_{iter}		n_{iter}	
		$f_c = 0$	$f_c = 0.1$	$f_c = 0$	$f_c = 0.1$
0.02 - (1)	1	15	25	11	15
	2	11	17	8	11
0.2 - (10)	1	6	9	7	7
	2	5	9	5	6
0.5 - (25)	1	6	8	6	7
	2	5	9	4	5
1.0 - (50)	1	6	42	6	7
	2	4	50	4	5
	3	–	29	–	–

6 Conclusions

A finite strain elastic-viscoplastic numerical framework was developed and implemented into the FE context. The overall approach is intended to simulate high velocity plastic deformation processes in which loading history effects have to be considered. The main goal was to provide an adequate and computationally efficient numerical tool for high strain

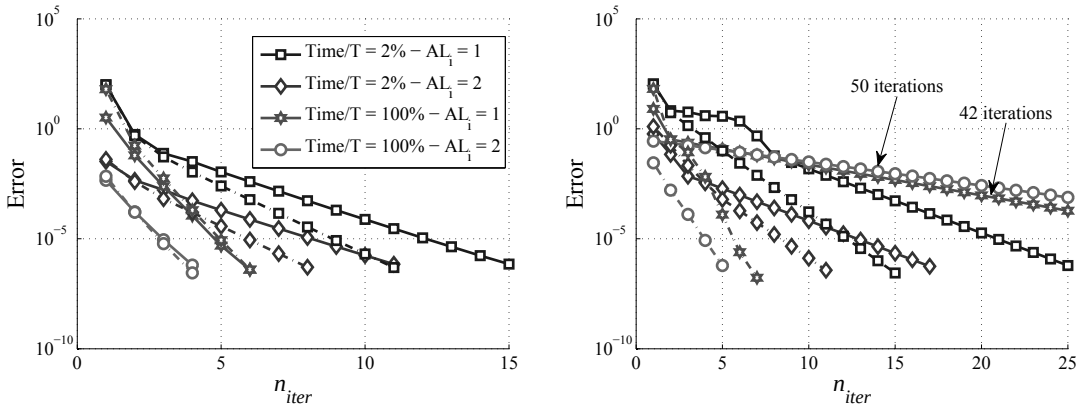

Figure 14: Convergence curves for *quasi*-static (solid lines) and high strain rate $\left(K = 9 \times 10^3\,\mathrm{s}^{-1}\right)$ (dash-doted lines) cases: (a) Frictionless compression; (b) Frictional compression.

rate straining of metals. The accuracy of constitutive modeling and related numerical procedure was assessed by means of homogeneous decremental strain rate and constant strain rate loading followed by stress relaxation testing, and global analysis consisting of a billet upsetting considering friction contact conditions. The loading process in the latter analysis is also defined by an initial constant loading rate stage followed by a stress relaxation phase. All these analysis have demonstrated the capabilities of the constitutive and numerical modeling to properly capture the main features of strain rate history effects on material and structural response of elastic-viscoplastic media. The algorithm convergence analyzes emphasized the good performance and robustness of numerical procedure. The numerical results obtained in this paper contribute to the understanding of high strain rate processes while encouraging for future developments in high strain rate material modeling.

Acknowledgements

The author Tiago dos Santos wishes to acknowledge the doctoral scholarship support of *CAPES*, Coordenação de Aperfeiçoamento de Pessoal de Nível Superior of Brazil. Process number BEX 7023/15-4. The author Rodrigo Rossi wishes to acknowledge the support of *CNPq*, Conselho Nacional de Desenvolvimento Científico e Tecnológico of Brazil. Grant number 304044/2015-6.

REFERENCES

[1] Klepaczko, J. Thermally activated flow and strain rate history effects for some polycrystalline f.c.c. metals. *Mater. Sci. Engng.* (1975) **18**:121–135.

[2] Chiem, C. and Duffy, J. Strain rate history effects and observations of dislocation substructure in aluminum single crystals following dynamic deformation. *Mater. Sci. Engng.* (1983) **57**:233–247.

[3] Tanner, A.B. and McDowell, D.L. Deformation, temperature and strain rate sequence experiments on OFHC Cu. *Int. J. Plast.* (1999) **15**:375–399.

[4] Huang, F. and Tao, N. Effects of strain rate and deformation temperature on microstructures and hardness in plastically deformed pure aluminum. *J. Mater. Sci. Tech.* (2011) **27**:1–7.

[5] Luo, Z., Zhang, H., Hansen, N. and Lu, K. Quantification of the microstructures of high purity nickel subjected to dynamic plastic deformation. *Acta Mater.* (2012) **60**:1322–1333.

[6] Follansbee, P. and Kocks, U. A constitutive description of the deformation of copper based on the use of the mechanical threshold stress as an internal state variable. *Acta Metall.* (1988) **36**:81–93.

[7] Nemat-Nasser, S. and Li, Y. Flow stress of f.c.c. polycrystals with application to OFHC Cu. *Acta Mater.* (1998) **46**:565–577.

[8] Gao, C. and Zhang, L. Constitutive modelling of plasticity of fcc metals under extremely high strain rates. *Int. J. Plast.* (2012) **32-33**:121–133.

[9] Rodríguez-Martínez, J., Rodríguez-Millán, M., Rusinek, A. and Arias A. A dislocation-based constitutive description for modeling the behavior of FCC metals within wide ranges of strain rate and temperature. *Mech. Mater.* (2011) **43**:901–912.

[10] Nemat-Nasser, S., Ni, L. and Okinaka, T. A constitutive model for fcc crystals with application to polycrystalline OFHC copper. *Mech. Mater.* (1998) **30**:325–341.

[11] Lebensohn, R. and Tomé, C. A self-consistent anisotropic approach for the simulation of plastic deformation and texture development of polycrystals: Application to zirconium alloys. *Acta Metall. Mater.* (1993) **41**:2611–2624.

[12] Roters, F., Eisenlohr, P., Hantcherli, L., Tjahjanto, D., Bieler, T. and Raabe, D. Overview of constitutive laws, kinematics, homogenization and multiscale methods in crystal plasticity finite-element modeling: Theory, experiments, applications. *Acta Mater.* (2010) **58**:1152–1211.

[13] Rusinek, A. and Jankowiak, T. *Constitutive Relations under Impact Loadings: Experiments, Theoretical and Numerical Aspects*, chap. Dynamic Behavior of Materials. Constitutive Relations and Applications. Springer Vienna: Vienna, (2014) 87–135.

[14] Bodner., S.R. and Rubin, M.B. Modeling of hardening at very high strain rates. *J. Appl. Phys.* (1994) **76**:2742–2747.

[15] Molinari, A. and Ravichandran, G. Constitutive modeling of high-strain-rate deformation in metals based on the evolution of an effective microstructural length. *Mech. Mater.* (2005) **37**:737–752.

[16] Durrenberger, L., Molinari, A. and Rusinek, A. Internal variable modeling of the high strain-rate behavior of metals with applications to multiphase steels. *Mater. Sci. Engng. A-Struct.* (2008) **478**:297–304.

[17] Rodríguez-Martínez, J., Rusinek, A. and Klepaczko, J. Constitutive relation for steels approximating quasi-static and intermediate strain rates at large deformations. *Mech. Res. Commun.* (2009) **36**:419–427.

[18] Simo, J.C. and Hughes, T.J.R. *Computational Inelasticity*. Interdisciplinary applied mathematics: Mechanics and materials, Springer, (1998).

[19] de Souza Neto, E.A, Perić, D. and Owen, D.R.J. *Computational Methods for Plasticity: Theory and Applications*. John Wiley & Sons, (2008).

[20] Lush, A., Weber, G. and Anand, L. An implicit time-integration procedure for a set of internal variable constitutive equations for isotropic elasto-viscoplasticity. *Int. J. Plast.* (1989) **5**:521–549.

[21] Weber, G. and Anand, L. Finite deformation constitutive equations and a time integration procedure for isotropic, hyperelastic-viscoplastic solids. *Comput. Meth. Appl. Mech. Engng.* (1990) **79**:173–202.

[22] Zaera, R. and Fernández-Sáez, J. An implicit consistent algorithm for the integration of thermoviscoplastic constitutive equations in adiabatic conditions and finite deformations. *Int. J. Solids Struct.* (2006) **43**:1594–1612.

[23] Mourad, H., Bronkhorst, C., Addessio, F., Cady, C., Brown, D., Chen, S., Gray III, G.T. Incrementally objective implicit integration of hypoelastic-viscoplastic constitutive equations based on the mechanical threshold strength model. *Comput. Mech.* (2014) **53**:941–955.

[24] Lee, E.H. Elastic-plastic deformation at finite strains. *J. Appl. Mech.* (1969) **36**:1–6.

[25] Mandel, J. *Plasticité classique et viscoplasticité: course held at the Department of Mechanics of Solids, September-October, 1971*. Courses and lectures - International Centre for Mechanical Sciences, Springer-Verlag, (1972).

[26] dos Santos, T., Rosa, P.A., Maghous, S. and Rossi, R. A simplified approach to high strain rate effects in cold deformation of polycrystalline FCC metals: Constitutive formulation and model calibration. *Int. J. Plast.* (2016) **82**:76–96.

[27] Perzyna P. Thermodynamic theory of viscoplasticity. Elsevier, (1971) 313–354.

[28] Perić D. On a class of constitutive equations in viscoplasticity: Formulation and computational issues. *Int. J. Num. Meth. Engng.* (1993) **36**:1365–1393.

[29] Ristinmaa, M. and Ottosen, N.S. Viscoplasticity based on an additive split of the conjugated forces. *Eur. J. Mech. A-Solids.* (1998) **17**:207–235.

[30] Alfano, G., Angelis, F.D. and Rosati, L. General solution procedures in elasto/viscoplasticity. *Comput. Meth. Appl. Mech. Engng.* (2001) **190**:5123–5147.

[31] Perzyna, P. Fundamental problems in viscoplasticity. Elsevier, (1966) 243–377.

[32] Wang, W.M., Sluys, L.J. and de Borst, R. Viscoplasticity for instabilities due to strain softening and strain-rate softening. *Int. J. Num. Meth. Engng.* (1997) **40**:3839–3864.

[33] Ristinmaa, M. and Ottosen, N.S. Consequences of dynamic yield surface in viscoplasticity. *Int. J. Solids Struct.* (2000) **37**:4601–4622.

[34] Eterovic, A.L. and Bathe, K.J. A hyperelastic-based large strain elasto-plastic constitutive formulation with combined isotropic-kinematic hardening using the logarithmic stress and strain measures. *Int. J. Num. Meth. Engng.* (1990) **30**:1099–1114.

[35] Jordan, J., Siviour, C., Sunny, G., Bramlette, C. and Spowart, J. Strain rate-dependant mechanical properties of OFHC copper. *J. Mater. Sci.* (2013) **48**:7134–7141.

[36] Mandel, J. Equations constitutives et directeurs dans les milieux plastiques et viscoplastiques. *Int. J. Solids Struct.* (1973) **9**:725–740.

[37] Lubliner, J. A maximum-dissipation principle in generalized plasticity. *Acta Mech.* (1984) **52**:225–237.

[38] Coleman, B.D. and Gurtin, M.E. Thermodynamics with Internal State Variables. *Rep. Prog. Phys.* (1967) **47**:597–613.

[39] Rice J. Inelastic constitutive relations for solids: An internal-variable theory and its application to metal plasticity. *J. Mech. Phys. Solids.* (1971) **19**:433–455.

[40] Lubliner, J. On the thermodynamic foundations of non-linear solid mechanics. *Int. J. Nonlinear Mech.* (1972) **7**:237–254.

[41] Gurtin, M., Fried, E. and Anand, L. *The Mechanics and Thermodynamics of Continua*. The Mechanics and Thermodynamics of Continua, Cambridge University Press, (2010).

[42] Voce, E. The relationship between stress and strain for homogeneous deformation. *J. Inst. Metals.* (1948) **74**:537–562.

[43] Bonet, J. and Wood, R. *Nonlinear Continuum Mechanics for Finite Element Analysis*. Cambridge University Press, (1997).

[44] Klepaczko, J. and Chiem, C. On rate sensitivity of f.c.c. metals, instantaneous rate sensitivity and rate sensitivity of strain hardening. *J. Mech. Phys. Solids.* (1986) **34**:29–54.

[45] Rashid, M.M., Gray, G.T. and Nemat-Nasser, S. Heterogeneous deformations in copper single crystals at high and low strain rates. *Philos. Mag. A.* (1992) **65**:707–735.

[46] Rossi, R., Alves, M.K. and Al-Qureshi, H.A. A total lagrangian framework for simulation of powder compaction process based on a smooth three-surface cap model and a mesh-free method. *Int. J. Num. Meth. Engng.* (2008) **75**:1457–1491.

[47] Rossi, R., Alves, M.K. and Al-Qureshi, H.A. An element-free galerkin method for metal forming simulations. *Engng. Comput.: Int. J. Comput. Aided Engng.* (2009) **26**:327–346.

[48] Follansbee, P.S. High strain rate deformation of FCC metals and alloys. *Metallurgical Applications of Shock-Wave and High-Strain Rate Phenomena*, Murr LE, Staudhammer KP, , Meyers MA (eds.). Marcel Dekker Inc.: New York, (1986) 451–479.

A Tangent quantities for return mapping algorithm

The return mapping algorithm is used to solve the nonlinear equations (43), (44) and (45), making use of an iterative procedure, such as the *Newton-Raphson* algorithm. In this context, some tangent quantities have to be evaluated. The system of nonlinear linear equations to be solved can be set as

$$f_1 = \left\| \bar{\boldsymbol{\tau}}^{D^{trial}}_{n+1} \right\| - \Delta\lambda 2\mu - \sqrt{\frac{2}{3}} \left(\sigma_y + A_{n+1}\right) - \bar{\Theta}^{-1}\left(\Delta\lambda, A_{n+1}\right) = 0, \tag{61}$$

$$f_2 = A_{n+1} - A_n - A_{\infty_{n+1}} c\sqrt{\frac{2}{3}}\Delta\lambda - \left[A_{\infty_{n+1}}\left(1 + c\epsilon_n\right) - A_n\right]\left[1 - \exp\left(-\delta\sqrt{\frac{2}{3}}\Delta\lambda\right)\right] = 0, \tag{62}$$

$$f_3 = A_{\infty_{n+1}} - A^{lwr}_{\infty} - \left[\frac{1}{\Delta t}\left(\frac{\sqrt{\frac{2}{3}}\Delta\lambda - \Delta t\dot{\epsilon}_{lwr}}{\dot{\epsilon}_{up} - \dot{\epsilon}_{lwr}}\right)\right]^{\xi}\left(A^{up}_{\infty} - A^{lwr}_{\infty}\right) = 0, \tag{63}$$

where involved unknowns are $\left\{\Delta\lambda, A_{n+1}, A_{\infty_{n+1}}\right\}$. Accordingly, the tangent terms are defined by

$$\frac{\partial f_1}{\partial\Delta\lambda} = -2\mu - \frac{\partial\bar{\Theta}^{-1}}{\partial\Delta\lambda}, \tag{64}$$

$$\frac{\partial f_2}{\partial\Delta\lambda} = -\sqrt{\frac{2}{3}}A_{\infty_{n+1}}c - \sqrt{\frac{2}{3}}\delta\left[A_{\infty_{n+1}}\left(1 + c\epsilon_n\right) - A_n\right]\exp\left(-\delta\sqrt{\frac{2}{3}}\Delta\lambda\right), \tag{65}$$

$$\frac{\partial f_3}{\partial\Delta\lambda} = -\sqrt{\frac{2}{3}}\frac{\xi}{\Delta t}\left[\frac{1}{\Delta t}\left(\frac{\sqrt{\frac{2}{3}}\Delta\lambda - \Delta t\dot{\epsilon}_{lwr}}{\dot{\epsilon}_{up} - \dot{\epsilon}_{lwr}}\right)\right]^{\xi-1}\left(\frac{A^{up}_{\infty} - A^{lwr}_{\infty}}{\dot{\epsilon}_{up} - \dot{\epsilon}_{lwr}}\right), \tag{66}$$

$$\frac{\partial f_1}{\partial A_{n+1}} = -\sqrt{\frac{2}{3}} - \frac{\partial \bar{\Theta}^{-1}}{\partial A_{n+1}}, \tag{67}$$

$$\frac{\partial f_2}{\partial A_{n+1}} = 1, \quad \frac{\partial f_3}{\partial A_{n+1}} = 0, \quad \frac{\partial f_1}{\partial A_{\infty_{n+1}}} = 0, \quad \frac{\partial f_3}{\partial A_{\infty_{n+1}}} = 1, \tag{68}$$

$$\frac{\partial f_2}{\partial A_{\infty_{n+1}}} = -c\sqrt{\frac{2}{3}}\Delta\lambda - (1 + c\epsilon_n)\left[1 - \exp\left(-\delta\sqrt{\frac{2}{3}}\Delta\lambda\right)\right]. \tag{69}$$

From Eq. (18) we have the derivatives

$$\frac{\partial \bar{\Theta}^{-1}}{\partial \Delta\lambda} = \sqrt{\frac{2}{3}}\left(\sigma_y + A_{n+1}\right)\frac{1}{m}\frac{\vartheta}{\Delta t}\left(1 + \vartheta\frac{\Delta\lambda}{\Delta t}\right)^{\frac{1}{m}-1}, \tag{70}$$

$$\frac{\partial \bar{\Theta}^{-1}}{\partial A_{n+1}} = \sqrt{\frac{2}{3}}\left[\left(1 + \vartheta\frac{\Delta\lambda}{\Delta t}\right)^{\frac{1}{m}} - 1\right]. \tag{71}$$

B Analytical consistent tangent operator

Evaluation of $\mathbb{D}^{vp}_{n+1}$ is obtained from linearization of Eqs. (37), (39), (45) and (44),

$$d\boldsymbol{E}^{e}_{n+1} + d\left(\Delta\lambda\right)\boldsymbol{N}_{\bar{\boldsymbol{\tau}}_{n+1}} + \Delta\lambda\frac{\partial \boldsymbol{N}_{\bar{\boldsymbol{\tau}}_{n+1}}}{\partial \bar{\boldsymbol{\tau}}_{n+1}} : d\bar{\boldsymbol{\tau}}_{n+1} = d\boldsymbol{E}^{e^{trial}}_{n+1} \tag{72}$$

$$\boldsymbol{N}_{\bar{\boldsymbol{\tau}}_{n+1}} : d\bar{\boldsymbol{\tau}}_{n+1} + N_{A_{n+1}} dA_{n+1} = \frac{\partial \bar{\Theta}^{-1}}{\partial \Delta\lambda} d\left(\Delta\lambda\right) + \frac{\partial \bar{\Theta}^{-1}}{\partial A_{n+1}} dA_{n+1} \tag{73}$$

$$\begin{aligned} dA_{n+1} \;=\; & \left[\left(1 + c\epsilon_n\right)\left(1 - \varphi\right) + c\sqrt{\frac{2}{3}}\Delta\lambda\right] dA_{\infty_{n+1}} + \ldots \\ & \ldots + \sqrt{\frac{2}{3}}\left\{\delta\left[A_{\infty_{n+1}}\left(1 + c\epsilon_n\right) - A_n\right]\varphi + A_{\infty_{n+1}} c\right\} d\left(\Delta\lambda\right) \end{aligned} \tag{74}$$

$$dA_{\infty_{n+1}} = \omega d\left(\Delta\lambda\right) \tag{75}$$

where

$$\frac{\partial \boldsymbol{N}_{\bar{\boldsymbol{\tau}}_{n+1}}}{\partial \bar{\boldsymbol{\tau}}_{n+1}} = \frac{1}{\left\|\bar{\boldsymbol{\tau}}^{D}_{n+1}\right\|}\left(\mathbb{I} - \frac{1}{3}\boldsymbol{I}\otimes\boldsymbol{I} - \boldsymbol{N}_{\bar{\boldsymbol{\tau}}_{n+1}}\otimes\boldsymbol{N}_{\bar{\boldsymbol{\tau}}_{n+1}}\right), \tag{76}$$

$$N_{A_{n+1}} = \frac{\partial f_{n+1}}{\partial A_{n+1}} = -\sqrt{\frac{2}{3}}, \tag{77}$$

$$\varphi = \exp\left(-\delta\sqrt{\frac{2}{3}}\Delta\lambda\right), \tag{78}$$

and

$$\omega = \sqrt{\frac{2}{3}}\frac{\xi}{\Delta t}\left(\frac{A^{up}_{\infty} - A^{lwr}_{\infty}}{\dot{\epsilon}_{up} - \dot{\epsilon}_{lwr}}\right)\left[\frac{1}{\Delta t}\left(\frac{\sqrt{\frac{2}{3}}\Delta\lambda - \Delta t\dot{\epsilon}_{lwr}}{\dot{\epsilon}_{up} - \dot{\epsilon}_{lwr}}\right)\right]^{\xi-1}. \tag{79}$$

Combining Eqs. (74) and (75) reads to

$$dA_{n+1} = \Lambda d\left(\Delta\lambda\right), \tag{80}$$

where

$$\begin{aligned}\Lambda &= \left[\left(1+c\epsilon_n\right)\left(1-\varphi\right)+c\sqrt{\frac{2}{3}}\Delta\lambda\right]\omega+\ldots \\ &\quad \ldots+\sqrt{\frac{2}{3}}\left\{\delta\left[A_{\infty_{n+1}}\left(1+c\epsilon_n\right)-A_n\right]\varphi+A_{\infty_{n+1}}c\right\}.\end{aligned} \tag{81}$$

Inserting Eq. (80) into Eq. (73) yields

$$\boldsymbol{N}_{\bar{\boldsymbol{\tau}}_{n+1}} : d\bar{\boldsymbol{\tau}}_{n+1} = \left[\frac{\partial\bar{\Theta}^{-1}}{\partial\Delta\lambda}+\left(\frac{\partial\bar{\Theta}^{-1}}{\partial A_{n+1}}-N_{A_{n+1}}\right)\Lambda\right] d\left(\Delta\lambda\right)$$

$$d\left(\Delta\lambda\right) = \frac{1}{\chi}\boldsymbol{N}_{\bar{\boldsymbol{\tau}}_{n+1}} : d\bar{\boldsymbol{\tau}}_{n+1}, \tag{82}$$

where

$$\chi = \left[\frac{\partial\bar{\Theta}^{-1}}{\partial\Delta\lambda}+\left(\frac{\partial\bar{\Theta}^{-1}}{\partial A_{n+1}}-N_{A_{n+1}}\right)\Lambda\right]. \tag{83}$$

Substitution of Eq. (82) in Eq. (72) provides

$$d\boldsymbol{E}^{e}_{n+1}+\left(\frac{1}{\chi}\boldsymbol{N}_{\bar{\boldsymbol{\tau}}_{n+1}} : d\bar{\boldsymbol{\tau}}_{n+1}\right)\boldsymbol{N}_{\bar{\boldsymbol{\tau}}_{n+1}}+\Delta\lambda\frac{\partial\boldsymbol{N}_{\bar{\boldsymbol{\tau}}_{n+1}}}{\partial\bar{\boldsymbol{\tau}}_{n+1}} : d\bar{\boldsymbol{\tau}}_{n+1} = d\boldsymbol{E}^{e^{trial}}_{n+1}. \tag{84}$$

Observing that $\left(\boldsymbol{A}\otimes\boldsymbol{G}\right):\boldsymbol{K} = \left(\boldsymbol{G}:\boldsymbol{K}\right)\boldsymbol{A}$, the above equation writes

$$d\boldsymbol{E}^{e}_{n+1}+\frac{1}{\chi}\left(\boldsymbol{N}_{\bar{\boldsymbol{\tau}}_{n+1}}\otimes\boldsymbol{N}_{\bar{\boldsymbol{\tau}}_{n+1}}\right) : d\bar{\boldsymbol{\tau}}_{n+1}+\Delta\lambda\frac{\partial\boldsymbol{N}_{\bar{\boldsymbol{\tau}}_{n+1}}}{\partial\bar{\boldsymbol{\tau}}_{n+1}} : d\bar{\boldsymbol{\tau}}_{n+1} = d\boldsymbol{E}^{e^{trial}}_{n+1}, \tag{85}$$

and from the elastic relationship $d\boldsymbol{E}^{e}_{n+1} = \mathbb{D}^{e^{-1}} : d\bar{\boldsymbol{\tau}}_{n+1}$ Eq. (85) can be rearranged as

$$\left(\mathbb{D}^{e^{-1}}+\Delta\lambda\frac{\partial\boldsymbol{N}_{\bar{\boldsymbol{\tau}}_{n+1}}}{\partial\bar{\boldsymbol{\tau}}_{n+1}}\right) : d\bar{\boldsymbol{\tau}}_{n+1}+\frac{1}{\chi}\left(\boldsymbol{N}_{\bar{\boldsymbol{\tau}}_{n+1}}\otimes\boldsymbol{N}_{\bar{\boldsymbol{\tau}}_{n+1}}\right) : d\bar{\boldsymbol{\tau}}_{n+1} = d\boldsymbol{E}^{e^{trial}}_{n+1}, \tag{86}$$

leading finally to

$$\mathbb{D}^{vp}_{n+1} = \frac{\partial\bar{\boldsymbol{\tau}}_{n+1}}{\partial\boldsymbol{E}^{e^{trial}}_{n+1}} = \left(\mathbb{D}^{e^{-1}}+\Delta\lambda\frac{\partial\boldsymbol{N}_{\bar{\boldsymbol{\tau}}_{n+1}}}{\partial\bar{\boldsymbol{\tau}}_{n+1}}+\frac{1}{\chi}\boldsymbol{N}_{\bar{\boldsymbol{\tau}}_{n+1}}\otimes\boldsymbol{N}_{\bar{\boldsymbol{\tau}}_{n+1}}\right)^{-1}. \tag{87}$$